

# Trajectories and energy transfer of saltating particles onto rock surfaces: Application to abrasion and ventifact formation on Earth and Mars

Nathan T. Bridges,<sup>1</sup> James Phoreman,<sup>2,3</sup> Bruce R. White,<sup>4</sup> Ronald Greeley,<sup>5</sup>  
Eric E. Eddlemon,<sup>2</sup> Gregory R. Wilson,<sup>1</sup> and Christine J. Meyer<sup>6</sup>

Received 17 December 2004; revised 25 August 2005; accepted 9 September 2005; published 7 December 2005.

[1] The interaction between saltating sand grains and rock surfaces is assessed to gauge relative abrasion potential as a function of rock shape, wind speed, grain size, and planetary environment. Many kinetic energy height profiles for impacts exhibit a distinctive increase, or kink, a few centimeters above the surface, consistent with previous field, wind tunnel, and theoretical investigations. The height of the kink observed in natural and wind tunnel settings is greater than predictions by a factor of 2 or more, probably because of enhanced bouncing off hard ground surfaces. Rebounded grains increase the effective flux and relative kinetic energy for intermediate slope angles. Whether abrasion occurs, as opposed to simple grain impact with little or no mass lost from the rock, depends on whether the grain kinetic energy ( $E_G$ ) exceeds a critical value ( $E_C$ ), as well as the flux of grains with energies above  $E_C$ . The magnitude of abrasion and the shape change of the rock over time depends on this flux and the value of  $E_G > E_C$ . Considering the potential range of particle sizes and wind speeds, the predicted kinetic energies of saltating sand hitting rocks overlap on Earth and Mars. However, when limited to the most likely grain sizes and threshold conditions, our results agree with previous work and show that kinetic energies are about an order of magnitude greater on Mars.

**Citation:** Bridges, N. T., J. Phoreman, B. R. White, R. Greeley, E. E. Eddlemon, G. R. Wilson, and C. J. Meyer (2005), Trajectories and energy transfer of saltating particles onto rock surfaces: Application to abrasion and ventifact formation on Earth and Mars, *J. Geophys. Res.*, 110, E12004, doi:10.1029/2004JE002388.

## 1. Introduction

### 1.1. Perspective

[2] Modification of rocks on planetary surfaces depends on the rates of physical and chemical weathering. Earth probably exhibits the greatest diversity and complex interplay of weathering processes in the solar system, with the dominant process varying strongly as a function of location and rock composition relative to ambient conditions. In its current climate, Mars is a much simpler but less understood weathering environment. The availability of any liquid water is at best minor, being relegated to possible transient melting that may produce features such as gullies [Malin and Edgett, 2000, 2001]. Other processes, such as impacts,

temperature cycling, and chemical alteration are, to the best of current understanding, very slow or intermittent. Partly because of the relative ineffectiveness of these processes and also the great age of most of the Martian surface [Tanaka *et al.*, 1992], aeolian abrasion is expected to play a prominent role in surface weathering. On a regional scale, the ability for the wind to move sand-sized material is demonstrated by abundant dunes and sand sheets found across the planet [Greeley *et al.*, 1992; Malin and Edgett, 2001], although any recent activity has been limited [Edgett and Malin, 2000; Zimbelman, 2000; Malin and Edgett, 2001]. A corresponding ability for aeolian erosion is seen in the form of yardangs [Ward, 1979; Malin and Edgett, 2001]. On Earth, yardangs commonly are characterized by undercuts at their bases [Greeley and Iversen, 1985], a form (see further discussion below) consistent with aeolian abrasion, as opposed to strictly deflation in the absence of blowing sand. Evidence for exhumation of buried craters and other topography is found in the northern plains, in craters with remnant mounds, and elsewhere [Malin and Edgett, 2001]. This process was probably dominated by aeolian erosion.

[3] Ventifacts are rocks that have been sculpted by windblown particles. On Earth, ventifacts are found in areas where there is or has been a supply of sand, winds of sufficient speed and shear stress to blow the sand, and

<sup>1</sup>Jet Propulsion Laboratory, Pasadena, California, USA.

<sup>2</sup>Department of Geological Sciences, Arizona State University at NASA-Ames Research Center, Moffett Field, California, USA.

<sup>3</sup>Now at BAE Systems, Los Angeles, California, USA.

<sup>4</sup>Department of Mechanical Engineering, University of California, Davis, Davis, California, USA.

<sup>5</sup>Department of Geological Sciences, Arizona State University, Tempe, Arizona, USA.

<sup>6</sup>Department of Geological Sciences, Ohio University, Athens, Ohio, USA.

insufficient vegetation to inhibit saltation. Ventifacts form when the collision of saltating sand is of sufficient kinetic energy in the lower tens of centimeters of the near-surface boundary layer to abrade rock over time. Rocks abraded by this mechanism become faceted. The facets commonly are separated by sharp keels, and have pitted, fluted, and grooved textures [Laity, 1995]. The orientation of the elongated pits, flutes, grooves, and facet dip slopes are aligned with the direction of the predominant near-surface winds, such that ventifacts can serve as paleowind indicators [Sharp, 1948; Laity, 1995]. Rocks interpreted as ventifacts have been seen on Mars, with some possible examples at the Viking sites [Binder et al., 1977; Mutch et al., 1977; Viking Lander Team, 1978; McCauley et al., 1979] and more definitive and abundant examples at the Pathfinder [Bridges et al., 1999] and Spirit [Greeley et al., 2004] sites. At the Opportunity site, some of the bedrock spherules have fairly unidirectional tails which have been interpreted as abrasion features [Squyres et al., 2004; Sullivan et al., 2005]. Possibly analogous differential erosion features are seen in ventifact localities on Earth and interpreted at the Pathfinder site [Bridges et al., 1999; Greeley et al., 2002]. On the basis of the old age of much of the Martian surface, integrated erosion rates, including net deflation of soils and abrasion of rocks, are very low, on the order of  $0.01\text{--}0.04\text{ nm yr}^{-1}$  since the Hesperian [Golombek and Bridges, 2000; Golombek et al., 2005]. Instantaneous erosion rates are likely much higher, such that the Martian surface we see today has been sculpted by rare, yet powerful high wind events.

## 1.2. Review of Literature and Current State of Understanding

### 1.2.1. Abrasion Studies

[4] Ventifacts have been identified on Earth (see the review paper by Laity [1994], with extensive references) and Mars [Bridges et al., 1999; Greeley et al., 2002]. Terrestrial field research has focused on documentation of ventifact characteristics [Laity, 1994, and references therein] and in situ experiments in which materials have been modified by naturally abrading sand [Sharp, 1964, 1980; Liu et al., 2003; Bridges et al., 2004]. The susceptibility of rocks and other natural materials to abrasion has been quantified on a relative scale from laboratory studies [Suzuki and Takahashi, 1981; Greeley et al., 1982]. Suzuki and Takahashi [1981] abraded rocks with a sand blaster and found that abrasion rate was proportional to particle kinetic energy and inversely proportional to rock compressive strength. Greeley et al. [1982] also measured rock abrasion, using a hopper and a rotating arm that slung sand against mounted targets set on the outer circumference of an enclosed chamber. A dimensionless abrasion susceptibility ( $S_a$ ) index was derived, defined as the ratio of mass loss from the target rock to the mass of sand impacted.  $S_a$  was quantified for a range of rock and sand types and impact angles. Greeley et al. [1982] found that  $S_a$  was proportional to kinetic energy. For crystalline rocks, low and high impact angles had greater susceptibilities compared to intermediate angles for crystalline rocks (i.e., a U-shaped curve in  $S_a$  versus impact angle space). Combining  $S_a$  with estimates for the frequency of winds ( $10^{-4}$  for  $25\text{--}30\text{ m s}^{-2}$ ) and sand flux ( $0.0324\text{ kg m}^{-1}\text{ s}^{-1}$ ) on Mars, they computed

relatively high abrasion rates of  $7.7\text{--}210\text{ }\mu\text{m yr}^{-1}$ . Although these rates are similar to terrestrial estimates of  $\sim 30\text{--}500\text{ }\mu\text{m yr}^{-1}$  based on field mass loss measurements [Sharp, 1980; Malin, 1985], the great age of exposed rocks and craters on Mars implies that continuous abrasion would erase these features relatively quickly over geologic time. Greeley et al. [1982] proposed periodic burial and exhumation or abrasion by relatively soft dust aggregates to reconcile the old surface age with the abrasion rates. The estimates also assumed a continuously available particle supply, which may not be the case. By combining estimates of material loss from soils and ventifacted rocks with the ages of the surfaces of the Pathfinder and Spirit landing sites, integrated erosion rates in at least these parts of Mars, and probably over much of the surface, have been on the order of tenths of a nanometer per year since the Hesperian [Golombek and Bridges, 2000; Golombek et al., 2005]. As discussed later in the paper, we consider abrasion a very ephemeral process under current Martian conditions, such that it is possible to have high abrasion rates over the short term that, when integrated over geologic time, are low.

### 1.2.2. Saltation Trajectory and Impact Studies

[5] Understanding aeolian abrasion requires knowledge of how sand moves in saltation and impacts rock surfaces. Bagnold [1941] predicted grain paths by modeling their angle as the arctangent of the terminal velocity over the wind velocity and assumed that rebounds from the ground were nearly elastic. This was verified by experiments in which grains were collected following rebound and by photographs with exposures long enough to show grain paths. However, this is only an approximation, as saltating grains rarely reach the velocity of the wind [Greeley et al., 1983]. Field and numerical studies of grain trajectories have been used to study accumulation and ablation zones on sloped surfaces, principally dunes [Tsoar et al., 1996; White and Tsoar, 1997]. Predicted saltation trajectories have been computed numerically for Martian conditions [White et al., 1976; White, 1979]. These studies predict that the lower atmospheric density on Mars requires higher friction speeds and freestream velocities than on Earth. Such analyses are complicated by the variability of the correlation between the drag coefficient ( $C_D$ ) and Reynold's number ( $Re$ ) for sand grains at Mars atmosphere dynamic viscosities, leading to some uncertainty in the ratio of drag to gravitational forces. The drag to gravity force ratio determines the degree to which vertical velocities of grains vary on Mars compared to Earth, thereby affecting predictions of particle concentration profiles within a saltation cloud.

[6] High-speed video of saltating grains under terrestrial conditions has proved useful to measure trajectories and speeds. These studies have been used to determine spin (Magnus) effects on particle lift [White and Schulz, 1977], accurate particle speeds as a function of height [White, 1982], saltation threshold [Phoreman, 2002], and dust storm triggering mechanisms [Phoreman, 2002]. The present study is the first, to our knowledge, that uses high-speed video to study the effect of sloped facets on impact angles and rebound trajectories.

## 1.3. Intent of This Work

[7] A critical component to understanding rock abrasion is knowing how sand moves naturally in saltation, and thereby

**Table 1a.** General Parameters for Saltation Calculations

Parameter	Units	Earth	Mars
Gravity	$\text{m s}^{-2}$	9.81	3.83
Roughness height	m	0.003	0.003
Sand density	$\text{kg m}^{-3}$	2650	3000
<i>atmospheric parameters:</i>			
Pressure	$\text{Pa, kg m}^{-1} \text{s}^{-2}$	$1.01 \times 10^5$	1000
Temperature	K	293	263
Specific heat	$\text{J kg}^{-1} \text{K}^{-1}, \text{m}^2 \text{s}^{-2} \text{K}^{-1}$	286.987	188.912
Density	$\text{kg m}^{-3}$	1.21	0.0201
Dynamic viscosity	$\text{kg m}^{-1} \text{s}^{-1}$	$1.14 \times 10^{-5}$	$1.33 \times 10^{-5}$
Kinematic viscosity	$\text{m}^2 \text{s}^{-1}$	$9.4 \times 10^{-6}$	$6.6 \times 10^{-4}$
Mean free path	m	$6.1 \times 10^{-8}$	$5.6 \times 10^{-6}$

impacts rocks, in a given planetary environment. The height, velocity, and kinetic energy of individual grains, and the distribution of these in a saltation cloud, vary as a function of wind speed, grain size, atmospheric density, gravity, and other factors. In this study we define representative trajectories for saltating particles in a saltation cloud, determine their kinetic energy as a function of impact angle with a target, and apply the results to constrain relative abrasion rates and rock morphologic evolution in an abrading environment on Earth and Mars. We begin with a discussion of methods, namely application of a numerical saltation code for estimating saltation cloud properties, and the interpretation of wind tunnel abrasion experiments and high speed video analysis of particles impacting faceted surfaces. The energy transfer between impacting sand and rock surfaces is evaluated to determine the potential for abrasion as a function of controlling parameters. We conclude with implications for terrestrial and Martian rock abrasion. We show that the rate of abrasion is strongly controlled by initial facet angle and that most rocks should abrade to a common gross geometry given sufficient time and availability of abrading particles. Under current climatic conditions, wind speeds above threshold produce saltating grains with kinetic energies about an order of magnitude greater on Mars compared to Earth. Given that rocks seen at the Martian landing sites, although exhibiting some ventifact characteristics, do not have this common geometry, we conclude that conditions conducive to abrasion were rare over the time period during which the rocks have been exposed to surface winds.

## 2. Methods

### 2.1. Numerical Models

[8] The numerical saltation code (written by co-author White) incorporates the fundamental physics of saltation

and follows the treatments discussed by *White et al.* [1976] and *White* [1979]. Readers are referred to these papers for a detailed discussion, with just an overview presented here. The equations of motion are solved for relevant planetary conditions (Tables 1a and 1b). Two particle densities were used. For the terrestrial simulation, density was set at  $2650 \text{ kg m}^{-3}$ , the standard value for quartz, the most common type of dune sand on Earth and the type used in the wind tunnel experiments. Recent MER results show that Martian soils are derived from mafic parents and that the sand component is basaltic [*Christensen et al.*, 2004; *Morris*, 2004; *Squyres et al.*, 2004; *Soderblom et al.*, 2004]. The predominate makeup of standard basalt is plagioclase ( $\sim 2000\text{--}2800 \text{ kg m}^{-3}$ ) and pyroxene ( $\sim 3200\text{--}3600 \text{ kg m}^{-3}$ ), giving a bulk basalt density of  $\sim 3000 \text{ kg m}^{-3}$ . Basalt is therefore used for the Martian simulations.

[9] Wind velocity as a function of height was computed from the well-known logarithmic profiles first applied in a saltation context by *Bagnold* [1941],

$$u(z) = (u_*/\kappa) \ln(z/z_0), \quad (1)$$

where  $u$  is the velocity at a given height  $z$ ,  $z_0$  is the aerodynamic roughness height where the velocity is 0,  $\kappa$  is a constant of proportionality (von Karman constant), set to 0.4, and  $u_*$  is the friction speed, or drag velocity. The friction speed is equal to the square root of the surface shear stress,  $\tau$ , divided by the atmospheric density,  $\rho$ , ( $[\tau/\rho]^{0.5}$ ). In the computations here, roughness height was set at 3 mm, a height recognized originally by *Bagnold* [1941] as the point at which wind velocities become invariant for two phase sand-airflow (this should not be confused with the roughness height of  $\sim 1/30$ th the particle diameter for fixed, immobile roughness elements in one phase, particle-free, flow). Wind

**Table 1b.** Trajectory Values for Saltation Calculations

Particle Size, $\mu\text{m}$	1.2-m Wind Speed, $\text{m s}^{-1}$	Planet	Weight (N) <sup>a</sup>	Friction Speed, $\text{m s}^{-1}$	Liftoff Velocity, $\text{m s}^{-1}$	Maximum Height, cm
150	10	Earth	$4.6 \times 10^{-8}$	0.67	0.41	1.2
150	25	Earth		1.66	1.50	5.7
150	50	Earth		3.33	3.23	11.5
600	10	Earth	$2.9 \times 10^{-6}$	0.67	0.10	0.3
600	25	Earth		1.66	0.81	3.6
600	50	Earth		3.33	2.04	14.3
150	25	Mars	$2.0 \times 10^{-8}$	1.66	0.69	4.7
150	50	Mars		3.33	1.70	17.6
600	25	Mars	$1.3 \times 10^{-6}$	1.66	0.27	1.5
600	50	Mars		3.33	0.85	8.1

<sup>a</sup>Assumes spherical sand.



speeds of 10, 25, and 50 m/s and 25 and 50 m/s for Earth and Mars, respectively, were used. Following equation (1), this gives friction speeds of 0.7, 1.7, and 3.3 m s<sup>-1</sup> for the three velocity cases. These friction speeds are consistent with terrestrial field measurements and theoretical treatments [Greeley and Iversen, 1985]. Lift is necessary to initially set the particles in motion [Einstein and El-Samni, 1949; Chepil, 1958, 1959; Saffman, 1965, 1968; Bagnold, 1973; Francis, 1973; White et al., 1976; White, 1986] and is parameterized as a coefficient necessary to raise a spherical grain from differential pressure about the particle surface [Saffman, 1965, 1968; White et al., 1976]. Appropriate lift and drag coefficients for Earth and Mars conditions were applied to two-dimensional equations of motion for the particles under the appropriate gravitational field [White et al., 1976; White, 1979, 1986]. The Martian case takes into account the effects of slip flow in the rarified atmosphere [White, 1979]. The  $x$  (horizontal) and  $z$  (vertical) positions of the particle were tracked in incremented time steps. Back points were initially calculated with the Runge-Kutta-Gill single-step method [Phoreman, 2002]. Accuracy was checked at each step and step size was changed accordingly.

[10] The results of the runs were particle position ( $x, z$ ) with time ( $t$ ). From these, horizontal and vertical velocities ( $dx/dt$  and  $dz/dt$ , respectively), vector velocities ( $v = [(dx/dt)^2 + (dz/dt)^2]^{0.5}$ ), trajectory angle ( $\text{atan}[dz/dx]$ ), and kinetic energy ( $mv^2/2$ ) were computed. As will be justified in detail below, the inverse of the vertical velocity ( $dt/dz$ ) for both the ascending and descending parts of the trajectory was used to compute the concentration with height for the hypothetical case in which all grains in a saltation cloud followed the same path as the single case modeled.

[11] Field and modeling studies show that collision of saltating grains into a granular bed and the resultant ejection of more grains downwind accounts for most particles in natural saltation [White and Schulz, 1977; Ungar and Haff, 1987]. In the only documented wind tunnel study (that we are aware of) of ejected grain dynamics, White and Schulz [1977] used high speed video to measure liftoff velocities of 350–710  $\mu\text{m}$  glass beads of a density of 2500 kg m<sup>-3</sup> in a wind tunnel under a freestream airflow of 10.3 m s<sup>-1</sup> and friction speed of 39.6 cm s<sup>-1</sup>. Liftoff velocities ranged from  $\sim 20$  to 200 cm s<sup>-1</sup> (data were plotted in 20 cm bins), with an average of  $69.3 \pm 32.5$  cm s<sup>-1</sup>. This is comparable to the vertical liftoff velocities found here (Tables 1a and 1b). The work of White and Schulz showed that liftoff velocity, liftoff angle, and particle spin, which induces lift, are the three most important factors determining the initial trajectories of particles ejected from a bed. In a theoretical study of saltation, Anderson and Hallet [1986] and Anderson [1986] modeled the probability density distribution of vertical liftoff speeds, proposing that the variability of this factor outweighed the contributions of the other two. They chose an exponential form of the liftoff distribution to match the experimental results of White and Schulz [1977] and assumed that all liftoff angles were 50° to horizontal (the mean value found by White and Schulz), and that averaging over many particles of various spin states gave results comparable to that assuming no spin. They then numerically integrated over the trajectories from such a

liftoff distribution, assuming, based on their fitting to the White and Schulz results, that the mean distribution equaled  $0.63u_*$  for all particle sizes and wind speeds. Their model yielded good fits and correlations to wind tunnel and field data reported in earlier references [Williams, 1964; Sharp, 1980].

[12] Although our computed trajectories are those induced from aerodynamic lift, not from collision by upwind particles, the liftoff velocities are similar for comparable conditions (Tables 1a and 1b). We therefore take the modeled trajectories and assume that they represent those resulting from the most probable liftoff speed. We then fit the results to the probability density equation of Anderson and Hallet [1986] in order to get realistic values of abrasion potential with height in a saltation cloud. This is presented in greater detail in section 3.5. Thus an inherent assumption in this work is that the predicted trajectories are similar to those induced by collision with a granular bed. Future experimental work that determines the liftoff conditions of particles from a granular bed for a broader range of conditions are clearly desired. Finally, neither our model, nor any other detailed analytical work in the published literature that we are aware of, incorporates the effects of impact saltation and bouncing off hard surfaces, such as rock or indurated soil, that is likely to increase the trajectory heights. This is discussed in further detail in section 4.1.

## 2.2. Wind Tunnel Experiments

### 2.2.1. Facility Overview

[13] All experiments used the Mars Surface Wind Tunnel (MARSWIT) operated by Arizona State University's Department of Geological Sciences and based at NASA's Ames Research Center, Moffett Field, California [Greeley et al., 1981]. An open-circuit boundary layer wind tunnel, it has dimensions of 13 m (length)  $\times$  1.2 m (width)  $\times$  0.9 m (height) and is contained within a 4000 m<sup>3</sup> sealed chamber. Both terrestrial and Martian pressures are maintainable. Low (Martian) atmospheric pressures down to 3.5 mb are achieved via a five-stage steam ejection plant. Winds are maintained via suction from a fan and motor system at the exit end of the tunnel and a gas injection system. Free-stream velocities up to 100 m s<sup>-1</sup> are possible at Martian pressures. Because Earth atmosphere at 10 mb and standard temperature has nearly the same density (0.0128 kg m<sup>-3</sup>) and viscosity ( $1.76 \times 10^{-5}$  Pa s) as 6 mb carbon dioxide at a typical Martian temperature of 263 K (0.0136 kg m<sup>-3</sup>,  $1.51 \times 10^{-5}$  Pa s), air is used instead of CO<sub>2</sub> [Phoreman, 2002]. At Earth standard pressures ( $\sim 1$  bar), winds up to 11 m s<sup>-1</sup> are achieved using the fan and motor system. Sand is fed through an adjustable, motorized hopper mounted on the top of the tunnel 1.3 m downwind from the air intake and flow straighteners. The hopper has a volume of  $\sim 0.03$  m<sup>3</sup> and holds about one standard bag (22.7 kg) of sand. Sand flux is controlled by the size of the opening at the bottom of the hopper and the flux can be accurately adjusted in real time. Targets are placed downwind of the hopper, with the distance depending on the type of investigation. As discussed below, experiments examining the effect of angled facets on grain rebound used wooden blocks placed 1.75 m downwind, where incoming trajectories were fairly predictable and consistent. To mea-

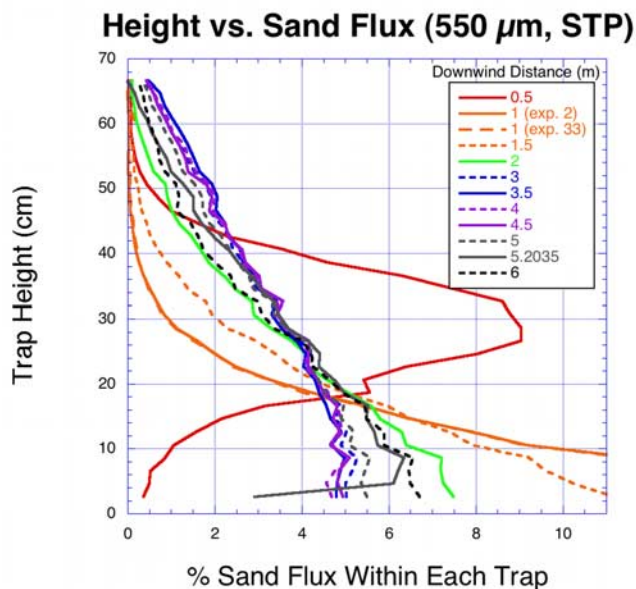


**Figure 1.** Sand flux versus height for a range of downwind distances as measured in the Mars Surface Wind Tunnel. Tests used 30 mesh (550- $\mu\text{m}$  mean opening size) quartz sand, dropped from a hopper, at Earth pressure, under a freestream wind speed of 9–11  $\text{m s}^{-1}$ . Sand was measured in 2-cm increments from a height of 2.6 to 66.6 cm above the tunnel floor. Distances are those from the hopper.

sure abrasion, soft targets were placed 4 m downwind, a distance at which a saltation cloud is developed. Instrumentation associated with the wind tunnel includes pressure and temperature sensors, wind velocity probes, humidity monitors, and photographic equipment.

### 2.2.2. Flux Versus Height Tests

[14] To verify the predicted particle trajectories, the sand distribution in MARSWIT for 30 mesh (550- $\mu\text{m}$  mean opening size) hopper-dropped particles at 11  $\text{m s}^{-1}$  at STP was measured by placing a stacked set of 33 sand traps at various downwind distances. These same traps were used in the first flux studies at MARSWIT more than 2 decades ago [Greeley *et al.*, 1982; White, 1982]. The same set of traps was used each run, with all parameters except the trap distance held constant among the runs. The traps measured sand intake every 2 cm from a height of 2.6 to 66.6 cm above the tunnel floor. By examining the height versus distance data, the point at which most of the particles reached the base of the tunnel and subsequently saltated downwind was determined (Figure 1). At 0.5 m from the hopper there is a pronounced peak at 30 cm, indicating that the majority of sand was in the process of falling from the hopper while being driven downstream by the wind. At 1.0 to 1.5 m downwind, the highest flux is at the bottom, indicating that a significant number of particles had reached the base of the tunnel. The height versus flux trend is more or less similar for all distances farther downwind, indicating that by this distance most of the particles had hit the floor and rebounded and thereafter were saltating across the floor, more or less emulating a sand cloud. This justified the use of a distance of 4 m downwind from the hopper for the placement of the abrasion targets.

### 2.2.3. Abrasion Experiments

[15] Because the numerical models make predictions of the kinetic energy flux in a saltation cloud as a function of wind speed, trajectory/impact angle, and atmospheric pressure, the model outputs were compared to wind tunnel tests in which mass lost from abradable targets was measured. The mass loss measurements for most of the terrestrial and some of the Martian experiments at a height of 20 cm were reported by Bridges *et al.* [2004]. Additional experiments performed for this paper were mass loss measurements at heights of 40 and 60 cm for terrestrial conditions and completion of the experimental matrix at 20 cm for Martian conditions. A detailed discussion of the targets, much of the experimental setup, and results at the time of writing of the earlier paper are discussed by Bridges *et al.* [2004]. In brief, the targets are composed of 60 (225  $\mu\text{m}$  mean) or 30 mesh dune sand embedded in a matrix made from gypsum paste and water. This material abraded in tens of minutes to hours in the experiments, thereby allowing a measurement of target mass loss within the sand cloud produced in the wind tunnel. Each target had three front faces with a length along the dip slope of 5 cm, oriented at angles of 90, 60, and 45° to the wind stream as seen from above [Bridges *et al.*, 2004, Figure 2]. These faces were sloped, as seen from the side, at angles of 90, 60, 45, 30, or 15° relative to horizontal. The targets were placed 4 m downwind of the hopper, with the height of the base generally at 20 cm. The hopper flux rate was 0.007  $\text{kg s}^{-1}$ . Measuring mass loss and angle changes as a function of time, hopper flux, and wind speed, the relative abrasion efficiency as a function of kinetic energy and trajectory angle were made. At Earth pressure, 108 experiments using various targets were completed at wind velocities of 11  $\text{m s}^{-1}$ . Of these, 18 experiments were run at heights of 40 cm and 18 at 60 cm. The Mars tests consisted of 57 experiments run at 35 and 47–58  $\text{m s}^{-1}$ , all at a height of 20 cm.

### 2.2.4. Impact Experiments

[16] To determine the effect of facet angle on trajectories of saltating grains, high speed video (HSV) was used to record particle positions over time. Five sand impact experiments, not including runs for calibrations or that yielded non-optimal results, were conducted at Earth pressure at freestream wind speeds of 11  $\text{m s}^{-1}$  using 30 mesh sand. All of these experiments were run at the standard hopper flux rate of 0.007  $\text{kg s}^{-1}$ . Five wooden block targets, one per experiment, were used. Each had a unique front facet angle relative to horizontal (approximately wind stream) of 90° (i.e., vertical), 60°, 45°, 30°, and 15° (i.e., nearly horizontal). The targets were painted black to minimize glare, thereby making the sand grains more apparent in the high speed video. They were mounted on a wooden plank, with the target bases 5.5 cm above the wind tunnel floor. The field of view of the HSV was  $\sim 20 \times 30$  cm, so that only a constrained cross section of the trajectory distribution in the tunnel could be monitored. This limitation dictated a precise placement of the targets in a region where sand impact was expected and flux sufficient to get proper trajectory statistics. The targets were therefore placed 1.75 m downwind from the hopper, a distance at which our numerical models predicted that typical 30 mesh hopper-dropped quartz sand grains would impact the targets (Figure 2). This is also the

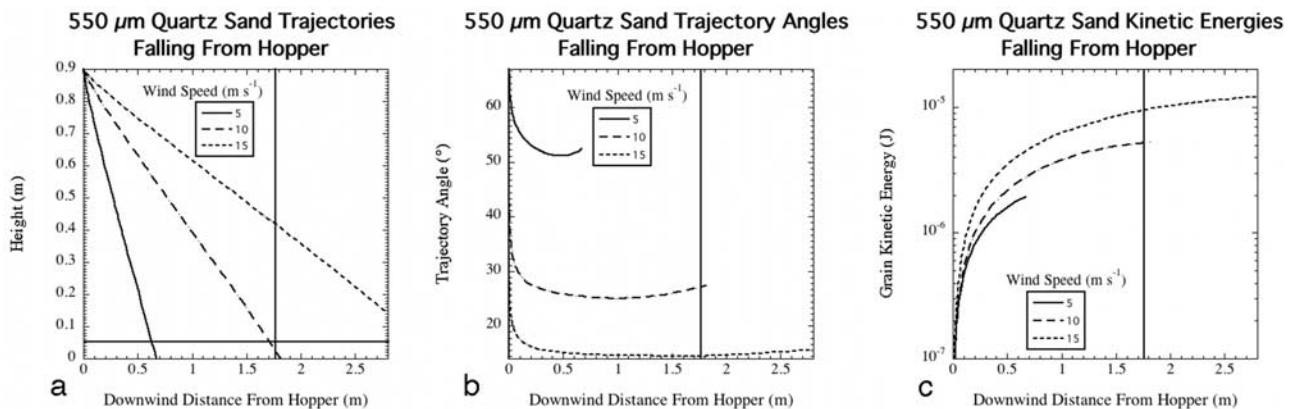


**Figure 2.** Plotted results for calculations of height, trajectory angle, and grain kinetic energy versus downwind distance for 30 mesh (550- $\mu\text{m}$  mean opening size) quartz grains for freestream winds of 5, 10, and 15  $\text{m s}^{-1}$ . The vertical line at 1.75 m in all graphs shows downwind distance from the hopper where impact experiments were conducted. The horizontal line at 5.5 cm in Figure 2a shows the elevation of the impact target bases.

distance at which the height versus flux profile showed a distinct peak in the lower few centimeters (Figure 1), indicating that many particles were in the vicinity of the floor for the first time prior to, or very shortly thereafter, bouncing downwind on their first saltation trajectory. This distance was chosen because (1) particle trajectories and kinetic energies are easily predictable and fairly simple and, as such, can be parameterized to other conditions; downwind the particles will have already hit the floor and will have a more mixed trajectory distribution, and (2) kinetic energies during the fall from the hopper are the highest at this point, thereby offering the best chance of observing high energy impact events like those seen in saltation/rock interactions in nature (Figure 2c). The predicted trajectory angle and kinetic energies/grain at 1.75 m are  $\sim 25^{\circ}$  and  $6 \times 10^{-6}$  J, respectively.

[17] The particle impacts were tracked with an NAC High Speed Video (HSV-1000) system mounted off to the side of the wind tunnel and viewed through Plexiglas on the tunnel walls. A Navitar 50 mm lens with a focal length of 0.6 m and f/stop rating of 0.95 was used. This provided a field of view of about  $20 \times 30$  cm when focused at the middle (as seen from the side) of a target. Six Halogen 1000-W bulbs illuminated the particles and target to provide sufficient light for high speed imaging. A grid of 1-cm squares was placed behind the targets to document position and velocity of the particles, with focus set at the midpoint of the targets. Video was shot at 1000 frames/second, with the exposure at 1/1000th of a second ("full open"), for a duration of about 15 s for each relevant experiment. An embedded chronometer recorded the relative time of each frame. The video was placed onto VHS tape at 30 frames/second so that  $1000/30 = 33$  s recorded 1 s of the experiments. The targets and centimeter grid were clearly seen in the VHS tape. By comparing the particle position on the grid to the chronometer time, the velocity and trajectories of representative particles were determined. Not all particles could be tracked completely through their trajectories in the field of view; many were partially or completely out of focus for the duration of the experiment. Therefore only visible, in-focus particles were

tracked, but these were sufficient to provide a statistical sample of all particle trajectories.

### 3. Results

#### 3.1. Numerical Trajectories and Kinetic Energies

[18] Predicted trajectories for the six terrestrial and four Martian cases are shown in Figure 3. The plots are exaggerated in the vertical dimension and are intended to illustrate the relative trajectory differences as a function of particle size, wind speed, and planetary environment. The resulting trajectory height is a complex combination of liftoff velocity, shear stress, particle size, and forces of lift, drag, and gravity that cannot be summarized easily from a few equations, hence the numerical modeling approach used here. A few generalities are apparent, however. Because the lift coefficient is proportional to friction speed [Saffman, 1968; White, 1986] for a given particle size and planetary environment, the fastest wind speeds result in trajectories with the greatest peak heights (Tables 1a and 1b). The trajectories closest to threshold for Earth and Mars ( $\sim 10$  and  $25 \text{ m s}^{-1}$ , respectively) are sufficient to raise sand just a few centimeters or less. From this analysis alone, it seems that abrasion on elevated rocks requires winds on the order of  $20 \text{ m s}^{-1}$  or more (at a height of 1.2 m) on Earth and about twice that much on Mars.

[19] The trajectory length depends on the height reached, the wind velocity, the coupling between the wind and sand, and the rate of fall, which depends on gravity and drag. This can also be illustrated in plotting height versus time, (Figure 4), in which the effects of the reduced Martian gravity manifest as shallower slopes on the descending part of the trajectory. When velocities in the trajectories are examined (Figure 5a), it can be seen that not only do particles in a higher speed wind move faster, as is intuitively obvious, but they also reach a greater fraction of the 1.2 m wind speed and the instantaneous wind speed (Figure 5b). The greater shear profile of higher speed winds results in particles reaching higher trajectories, such that they are aloft longer and get accelerated more. This is especially true for smaller 150- $\mu\text{m}$  grains



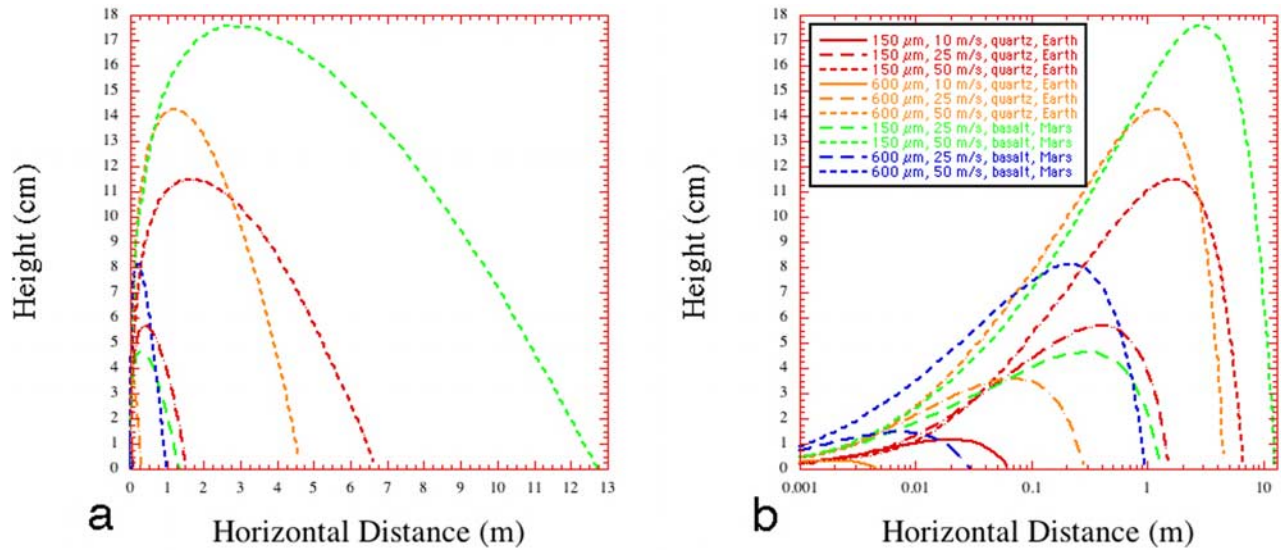


**Figure 3.** Plotted results for computations of height versus horizontal distance for representative trajectories for the particle sizes, wind speeds, and planetary environments shown. Particles are assumed to have a spherical shape. Linear  $x$  axis is shown in Figure 3a and a logarithmic one is shown in Figure 3b. Compare to Figure 4.

that are more easily accelerated by the wind. These results are consistent with earlier saltation modeling [Greeley *et al.*, 1983].

[20] Plotting kinetic energy (KE) as a function of height changes the shape and position of curves compared to height versus velocity space, given that KE varies with the cube of the particle size (for equivalent velocities) and the square of the velocity (for equivalent particle sizes) (Figure 6). Kinetic energy is generally greatest near or at the trajectory apex, where winds are the highest. After this point, any grain acceleration is relatively minor as it falls

through the velocity profile and is slowed down by drag. It is seen that 600- $\mu\text{m}$  particles in a  $50 \text{ m s}^{-1}$  wind on Earth have an order of magnitude greater kinetic energy than any other case. The other  $50 \text{ m s}^{-1}$  trajectories have similar kinetic energies of  $\sim 10^{-6} \text{ J/grain}$  at their apex, with the 600- $\mu\text{m}$  Mars case being slightly greater on the descending parts of its trajectory. From these curves alone, which is an incomplete analysis (see below), the predicted kinetic energies for typical dune sand composed of 100- to 200- $\mu\text{m}$  grains should be similar on the two planets for a given wind speed (either 25 and  $50 \text{ m s}^{-1}$ ). If a mixture

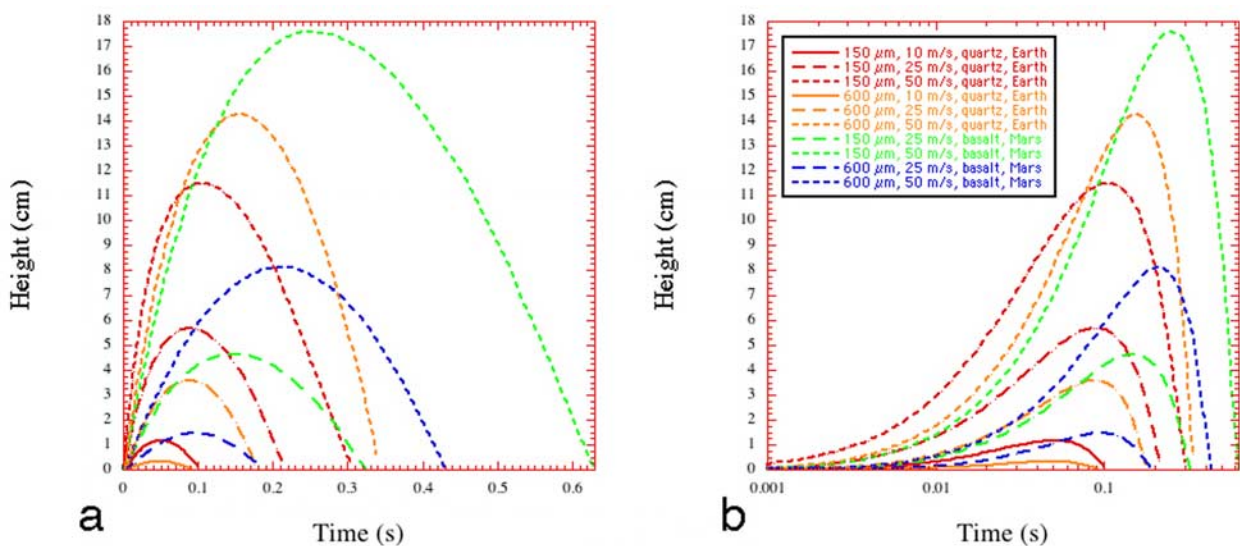


**Figure 4.** Plotted results for computations of height versus time for representative trajectories for the particle sizes, wind speeds, and planetary environments shown. Particles are assumed to have a spherical shape. Linear  $x$  axis is shown in Figure 4a and a logarithmic one is shown in Figure 4b. Compare to Figure 3.

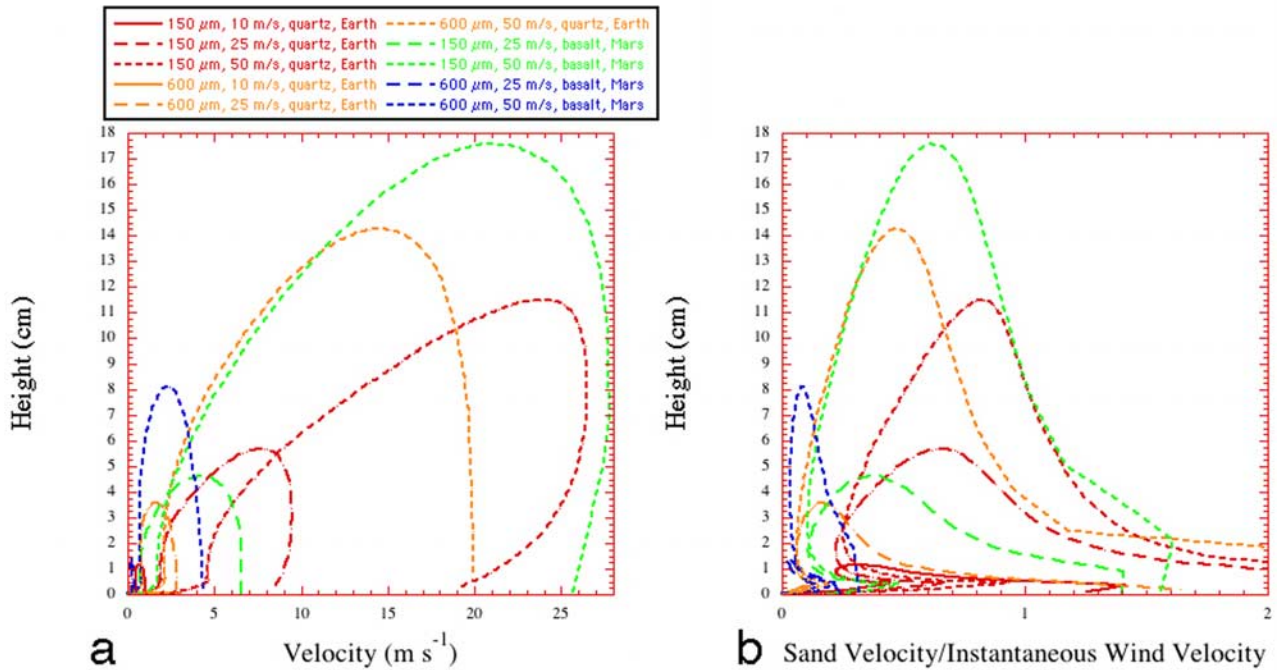


**Figure 5.** (a) Plotted results for computations of height versus particle velocity for representative trajectories for the particle sizes, wind speeds, and planetary environments shown. Particles are assumed to have a spherical shape. (b) Height versus the ratio of particle velocity to the instantaneous wind velocity (i.e., the predicted wind velocity at a given height, computed from equation (1)).

of grain sizes up to 600  $\mu\text{m}$  is available and fast winds of 50  $\text{m s}^{-1}$  are allowed, then kinetic energies are greater on Earth.

### 3.2. Trajectory Angle and Sloped Facets

[21] Analysis of abrasion must consider the orientation of rock surfaces relative to the saltation trajectories. The coordinate system we use is shown in Figure 7. Ascending trajectories are considered negative, and descending ones are positive. Only front side impacts are considered (e.g., those coming from the left in the diagram). Horizontal facets have a  $0^\circ$  angle and vertical ones  $90^\circ$ . The sign (+ or -) of the impact angle of a sand grain onto the facet is relative to the perpendicular ( $90^\circ$ ) from the facet face. Impact angles shallower than the  $90^\circ$  perpendicular are considered negative, varying from  $0^\circ$  for a grazing, upward sloping impact to  $-90^\circ$  when parallel to the perpendicular vector. Those steeper than the  $90^\circ$  perpendicular are considered positive, varying from  $+90^\circ$  when parallel to the perpendicular vector to the lowest possible impact angle on the positive side of  $90 - \theta$ , where  $\theta$  is the angle of the target. Because trajectory angles are generally  $\pm 10^\circ$  (see below), impact angles will be mostly negative for targets with facet angles  $< 80^\circ$ , whereas positive and negative impact angles close to  $90^\circ$  are expected for facets that are nearly perpendicular ( $90^\circ$ ) to the windstream.

[22] Trajectory angles can potentially vary from  $0^\circ$  to  $90^\circ$  in either the ascending or descending part of their path, although in practice are generally shallow. Consider a facet, varying from flat ( $\theta = 0^\circ$ ) to perpendicular ( $\theta = 90^\circ$ ). All descending trajectories will impact a facet, regardless of its orientation. The impact angle  $i$  that a descending trajectory

of angle  $\varphi$  makes with the facet is  $180 - \varphi - \theta$ . For ascending trajectories, only those angles that are shallower than the facet slope will impact, or  $i = -\theta - \varphi$  ( $-\varphi < \theta$ ; recall that  $\varphi$  is negative for ascending trajectories). The fraction of potential abrasion angles that a facet can see is therefore  $(90 + \theta)/180$  (Figure 8).

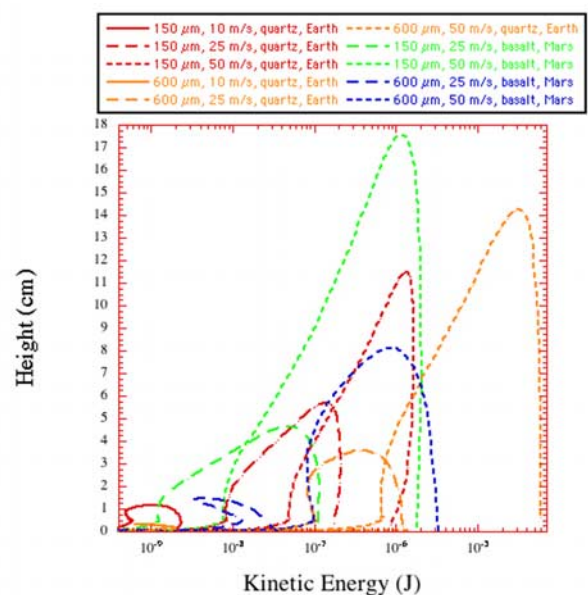


**Figure 6.** Plotted results for computations of height versus particle kinetic energy for a given point in the trajectory.



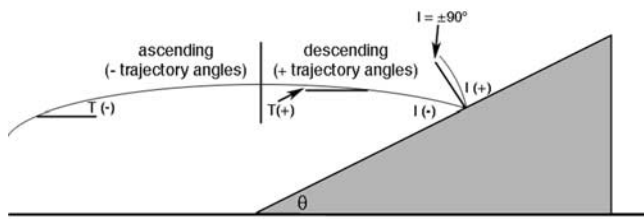


**Figure 7.** Geometry and nomenclature for angles in this paper.  $T$ , trajectory angle;  $I$ , impact angle;  $\theta$ , target or rock angle. Compare to Figure 8.

[23] To assess the potential range of impact angles for the different wind speed, sand size, and planetary conditions, trajectory angle for both ascending and descending paths is plotted as a function of dimensionless horizontal distance (beginning of path = 0, end of path = 1) (Figure 9a). Using a dimensionless distance scale allows an assessment of trajectory angles irrespective of hop length. Also shown on the plot are lines below which ascending trajectories will not impact targets of a given slope. As can be seen, most trajectories are flat except during their initial and final stages. Steeper angles are found for particles just barely above threshold that are not effectively entrained by the wind. Excluding these cases, most trajectories are dominated by the descending path when plotted against distance, even though particles spend about equal periods ascending and descending, with some variations due to the dependence of drag on velocity. This is shown in Figure 9b and illustrates a significant absence of ascending trajectories seen by shallow angled facets. As will be shown, this factors into the flux and kinetic energy versus height calculations.

[24] We next convert the trajectory angles to impact angles and consider the case for facets oriented 90, 60, 45, 30, 15, and 0° to the horizontal (Figures 10 and 11). This illustrates the range of impact angles expected for a sloped facet being abraded by saltating sand. This is plotted against dimensionless horizontal distance and dimensionless time, with the latter being more relevant for assessing the relative flux of various trajectories. For the 90° face, the plot is effectively the trajectory angle plot (Figure 9) flipped vertically, so that shallow trajectory angles are directly incident ( $i$  close to 90°) and steep trajectory angles become shallow impact angles. For this case, most impact angles are close to 90°. As facet angle decreases, impact angle approaches the negative of the facet angle. For example, the predominantly orthogonal angles that hit the 90° facet instead hit the 60° facet at an angle of -60°. For a 60° facet, any directly incident angles ( $i$  close to  $\pm 90^\circ$ ) are the same trajectories that for a 90° facet would be impacting at an angle of -60°. Also, as the angle becomes shallower, the plots show that the curves are truncated on the upper ends, illustrating that ascending trajectories are not being sampled.

### 3.3. Concentration Profiles

[25] We next examine the concentration profiles for the case in which all grains in saltation have the same trajectories. This must be done to subsequently weight the kinetic energy height profile. Note that once a full saltation cloud is developed, the concentration (particles per  $y$ - $z$  plane area)

profile should be time invariant and identical to the particle flux (particles per area per time) profile. Mass flux (mass per area per time) depends on the size and density of the particles and is applicable to the more complicated case where a bed of mixed sand is considered, a condition which is not modeled here.

[26] For the simplified single trajectory case, the concentration profile is proportional to the inverse of the vertical velocity ( $v_z^{-1} = dt/dz$ ). Implicit in this assumption is a suitably developed sand cloud of equal trajectories, with the grains in each trajectory at randomly spaced time intervals. Because the time spacing is random, the concentration with height is proportional to how long a grain spends in a given height bin, or  $v_z^{-1}$ . This is the same approach followed by *Anderson and Hallet* [1986]. The time spent in each 1 mm height bin ( $dt/dz$ ) for the ascending and descending parts of the trajectories was normalized to the total time of a given trajectory (e.g., the sum of the concentrations in the profile = 1). Plotting this against height illustrates the distribution of sand grains for a given saltation case (Figure 12a). The curves are smoothed over a running 4-mm bin to avoid discontinuities introduced by the resolution of the saltation code. The low vertical velocities at the apex of the trajectories cause the curves to exhibit a pronounced increase in concentration at the highest point. The magnitude of this increase is roughly inversely proportional to trajectory height. This is because higher trajectories have a more vertically distributed flux, so that the low vertical velocities at the saltation peak are a smaller overall fraction of the vertical velocity distribution compared to lower trajectories.

[27] We next examine the effect of angled facets on concentration profiles. As discussed above, ascending grains with trajectory angles ( $-\varphi$ ) less than the slope of the facet ( $\theta$ ) will not impact. Because computed concentrations in a given

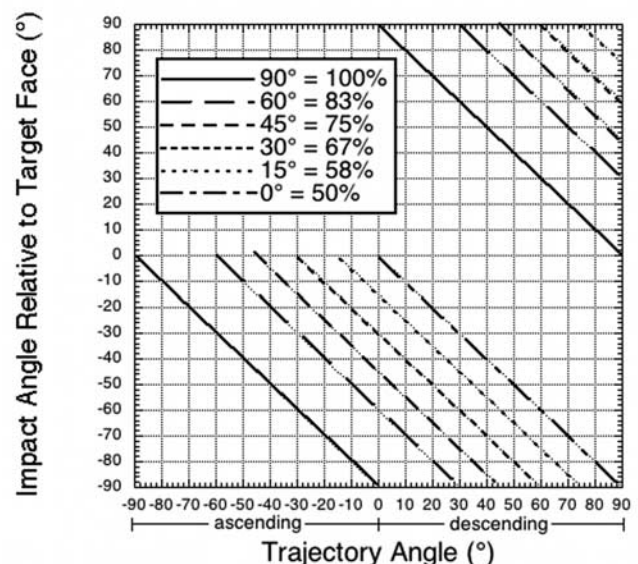


**Figure 8.** Diagram showing the relationship between impact angle relative to target face versus trajectory angle for six different target or rock facet angles. Also labeled are the percent of potential trajectory angles that can potentially impact a target of a given facet angle. Compare to Figure 7.

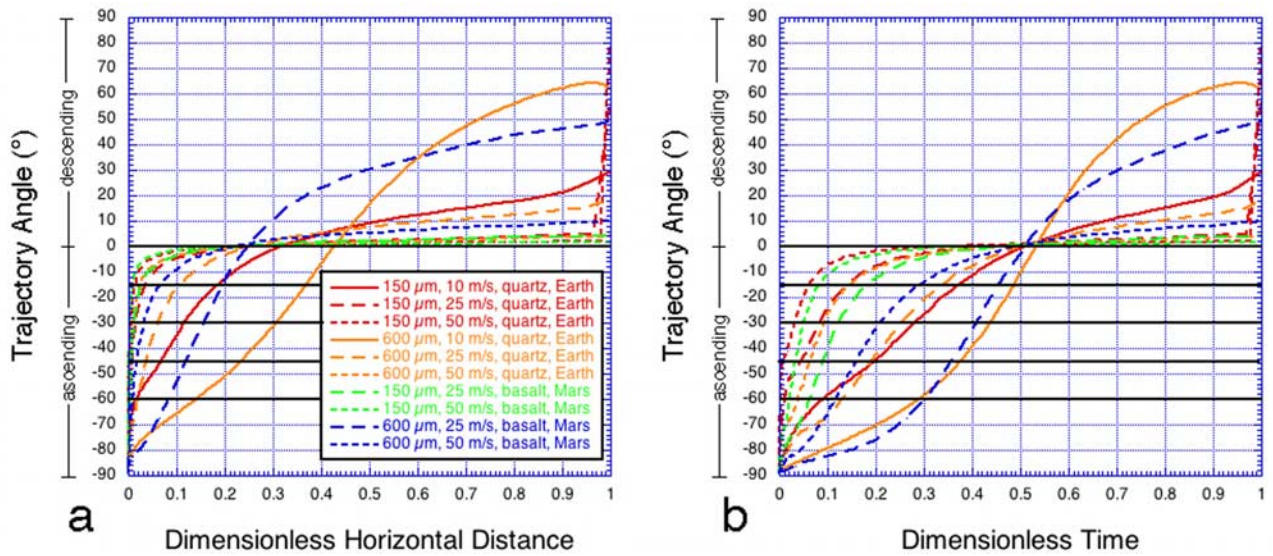


**Figure 9.** (a) Trajectory angle versus dimensionless horizontal distance (distance relative to that at the end of the trajectory) for representative trajectories that vary with the particle size, wind speed, and planetary environment. The dark horizontal lines demarcate minimum trajectory angles that a facet of a given angle can see (e.g., a facet angled  $60^{\circ}$  will not see trajectory angles  $< -60^{\circ}$ ). Compare to Figure 10. (b) Trajectory angle versus dimensionless time. Compare to Figure 11.

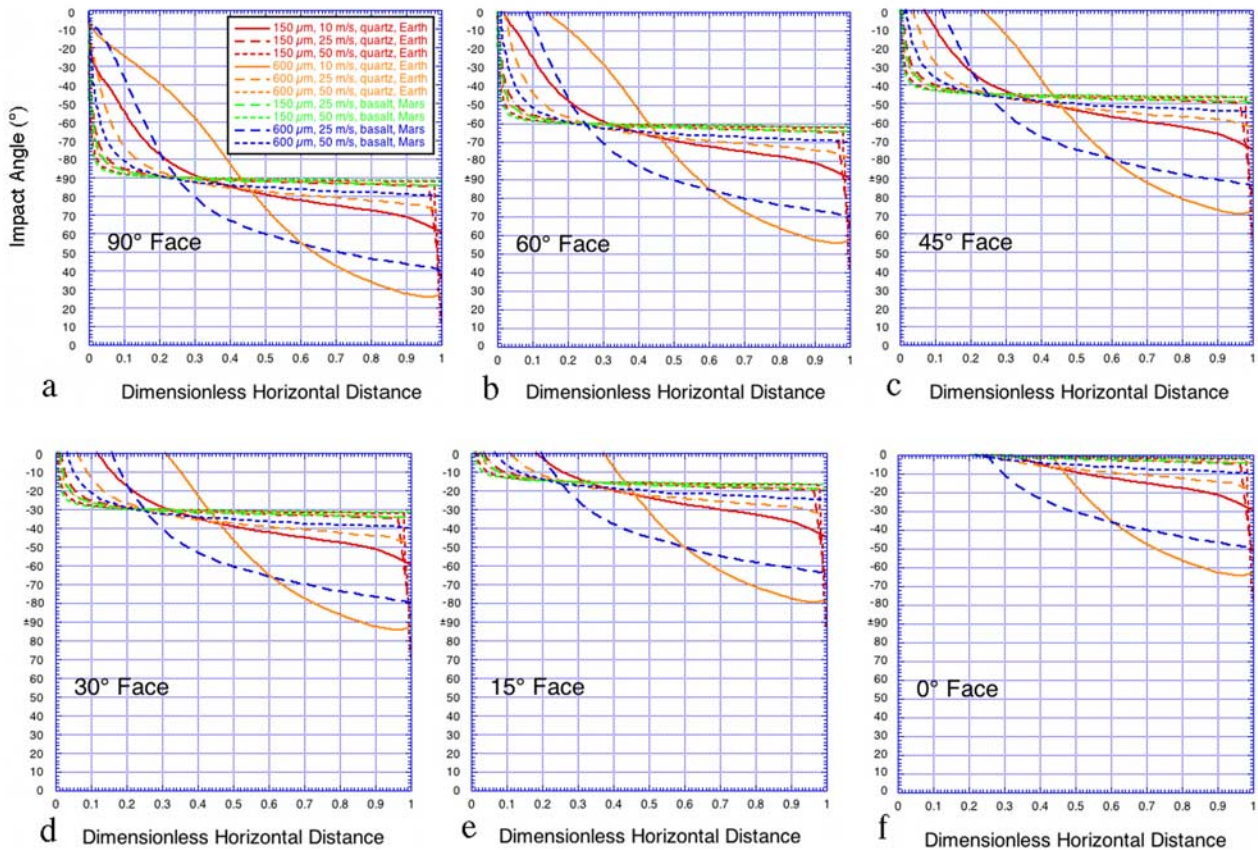


**Figure 10.** Impact angle versus dimensionless horizontal distance for a (a)  $90^{\circ}$  facet, (b)  $60^{\circ}$  facet, (c)  $45^{\circ}$  facet, (d)  $30^{\circ}$  facet, (e)  $15^{\circ}$  facet, and (f)  $0^{\circ}$  facet. Compare to Figure 9a.



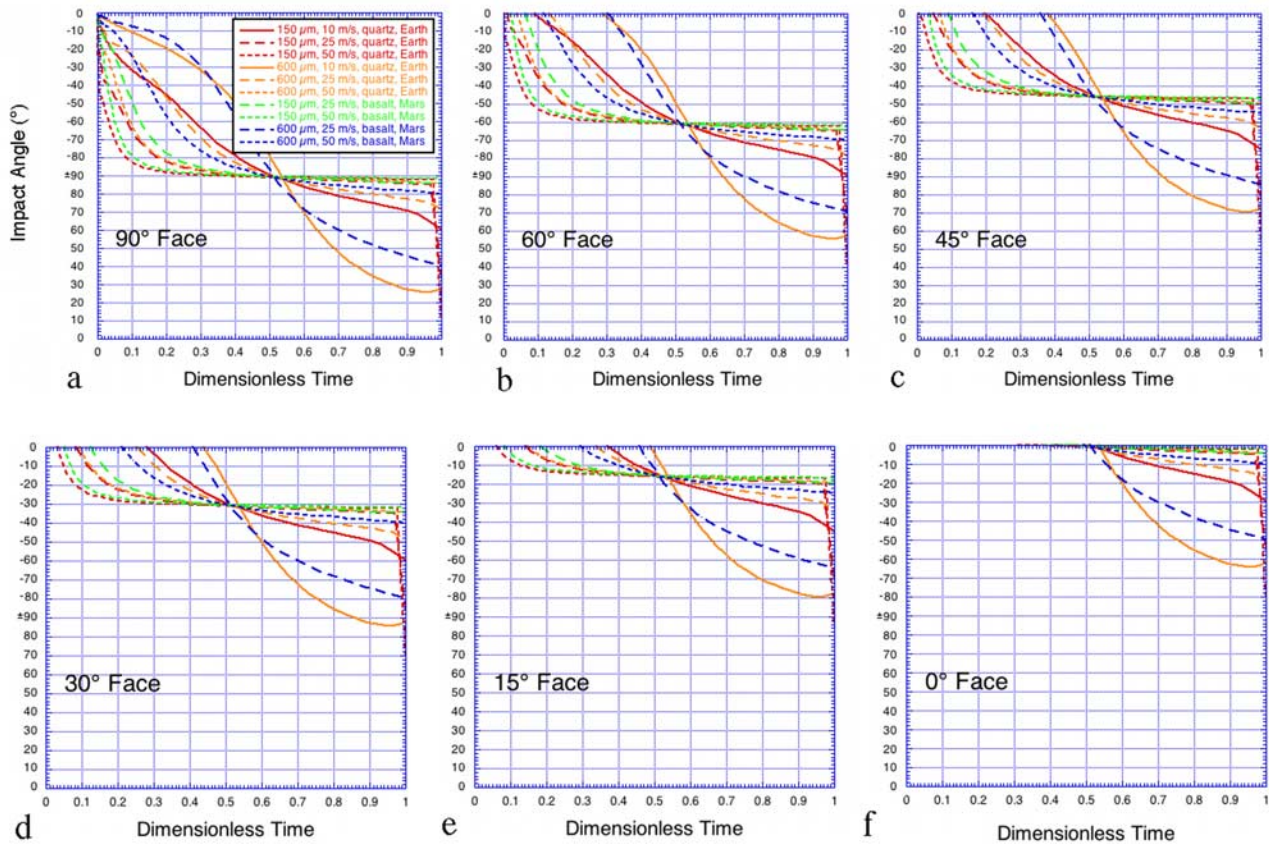


**Figure 11.** Impact angle versus dimensionless time for a (a) 90° facet, (b) 60° facet, (c) 45° facet, (d) 30° facet, (e) 15° facet, and (f) 0° facet. Compare to Figure 9b.

height bin take into account both ascending and descending grains, an adjustment must be made. We therefore removed any trajectories in which  $-\varphi$  was less than  $\theta$  and renormalized  $dt/dz$  from the time at which  $-\varphi = \theta$  to the end of the trajectory. Results are shown in Figures 12b–12f. These plots show that as facet slope becomes shallower, the particle concentration with height increases. This is due simply to the removal of ascending grains from the flux calculations, enhancing the relative contribution of very shallow grains at the top of the trajectory. This simple analysis, if believed (it will be shown subsequently as overly simplified) shows that concentration profiles increase more with height the shallower the facet angle.

### 3.4. Kinetic Energy Profiles

[28] We now compute the relative kinetic energy as a function of height in a sand cloud for the single trajectory case. The kinetic energies (Figure 6) in 1-mm-height bins for ascending and descending grains are multiplied by their relative concentration in the bin (Figure 12), with each bin divided between ascending and descending portions and applied to the appropriate kinetic energy in that part of the path. The curves are smoothed over a running 9-mm bin; this is done at twice the smoothing interval of the concentration profiles to account for deviations in the velocity profiles resulting from the saltation code resolution, which will affect KEs even more strongly because they are

proportional to  $v^2$ . The results (Figure 13) should not be interpreted as the actual KE of a grain at this height, but rather as a “relative” kinetic energy that factors in the concentration. For example, although the bottom of the descending part of the trajectories have relatively high KEs (Figure 6), the effective contribution averaged over a sand cloud is small because of the low concentrations of descending trajectories. There are three parts of the trajectory to consider. The ascending portion has KEs and concentrations that increase with height. The area near the apex has high KE and concentration. The descending portion has high KEs and concentrations that increase with height. The result is a relative KE that increases with height. Facet angle has a relatively minor effect on these curves because as this angle becomes shallower, only ascending grains, which generally have KEs an order of magnitude or two less than the descending ones at the same height, are removed.

[29] The next step in the analysis assesses the potential energy transfer into the rock. This is roughly proportional to the sine of the impact angle (although there are complications, as we consider in section 4), with high angles dissipating more momentum than glancing collisions [Routbort *et al.*, 1980; Scattergood and Routbort, 1983] (Figure 14). As facet angle becomes shallower, the impact angle of the relatively flat trajectories near the saltation path apex decreases, thereby lowering the amount



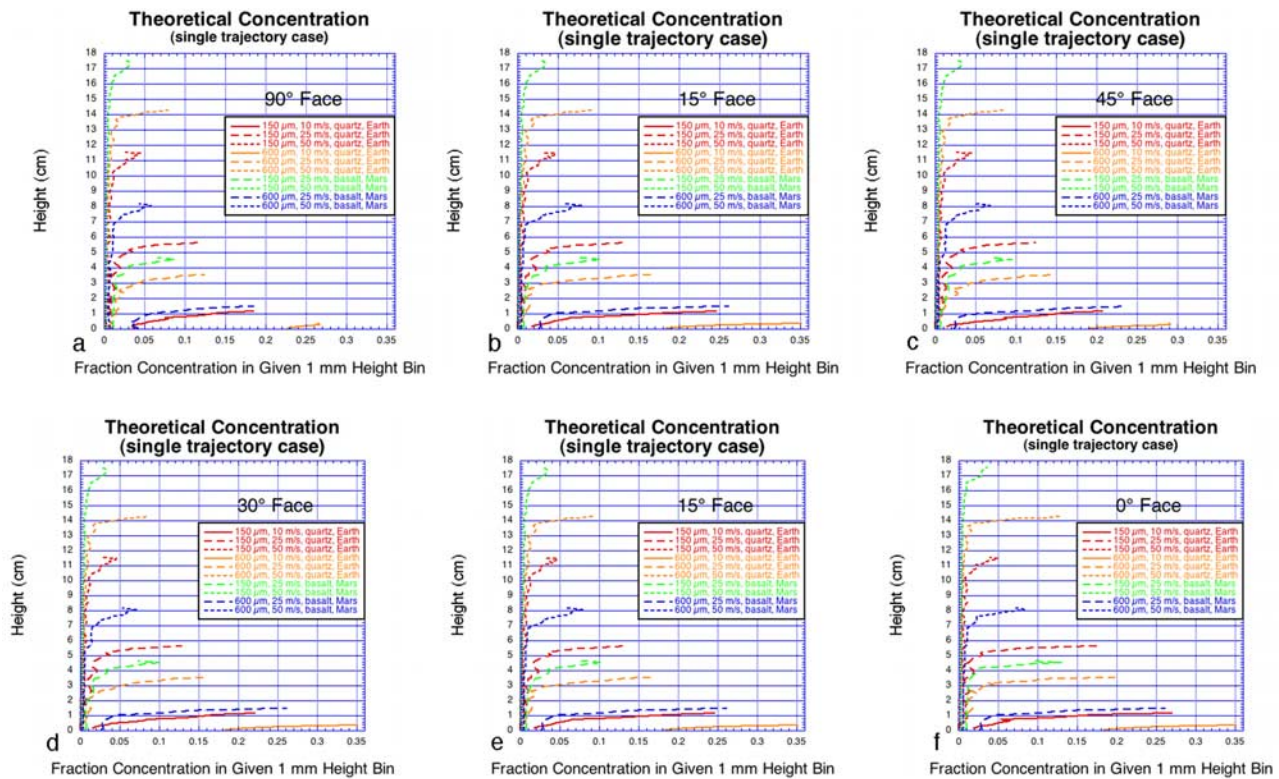


**Figure 12.** Height versus concentration for the single trajectory case as seen for a (a) 90° facet, (b) 60° facet, (c) 45° facet, (d) 30° facet, (e) 15° facet, and (f) 0° facet. The curves show some variations, which are due to the loss of ascending trajectories seen by a facet as facet angle gets shallower.

of kinetic energy that is transferred from the saltating grains into the rock. In the lower part of the saltation cloud the effect is variable and depends on the trajectory and facet angle. Because the relative kinetic energy is highest at the top of the cloud, the former process has the greatest effect. The overall result is that as facet angle decreases, overall kinetic energy and the change in KE with height decrease (note that the plots have a logarithmic  $x$  axis, so that facet angle changes from 90° to 15° reduces KE by a factor 2–3). These results predict: 1) Steep angled rocks should abrade more than shallow angled ones; and 2) differential abrasion with height is greatest on steep angled rocks.

### 3.5. Profiles Adjusted for Probabilistic Exponential Distribution

[30] Numerous measurements of flux and kinetic energy versus height in field and wind tunnel settings and for a range of particle sizes, mixtures, and speeds for sand and snow show that the curves are not as plotted here (Figures 12a and 13a). In these analyses, the peak in concentration or mass flux is found not at the top of the trajectory but rather near the surface and decreases exponentially with height [Bagnold, 1941; Sharp, 1964; Williams, 1964; Takeuchi, 1980; White, 1982; Greeley et al., 1983]. This has been attributed to ballistic collisions onto the particle bed that induce more grains into saltation that have a stochastic distribution of liftoff velocities and trajectories [Anderson and Hallet, 1986]. However, as the height versus flux tests reported here show (Figure 1), a

peak in concentration near the bottom of the profile results even for particles under a constant wind speed that are saltating over a surface free of loose particles.

[31] The lack of knowledge of the precise physics controlling the distribution of trajectories does not preclude using the results of experimental data. Following such a philosophy, Anderson and Hallet [1986] fitted an exponential probability density distribution to the trajectory data of White and Schulz [1977], yielding

$$P(v_0) = \exp(-v_0/v_{ave})/v_{ave}, \quad (2)$$

where  $v_0$  is the vertical liftoff velocity of interest and  $v_{ave}$  the mean vertical liftoff velocity. Anderson and Hallet [1986] showed that this equation yielded good fits to height versus concentration curves published by Williams [1964]. The profiles are imperfect in that they extend to infinity whereas the highest trajectories are, of course, at a finite height. However, the artificial concentrations at heights greater than that of the true maximum trajectory are a very small fraction of the total concentration integrated over all heights.

[32] The parameterization above does not take into account effects of lift and drag in different planetary environments. For a given particle size and planetary environment, liftoff velocity (defined here as the maximum  $z$  velocity in the lower shear layer) correlates to the maximum trajectory height (Tables 1a and 1b and Figure 15). To properly fit the exponential distribution to the single trajectory calculations, we substitute trajectory height

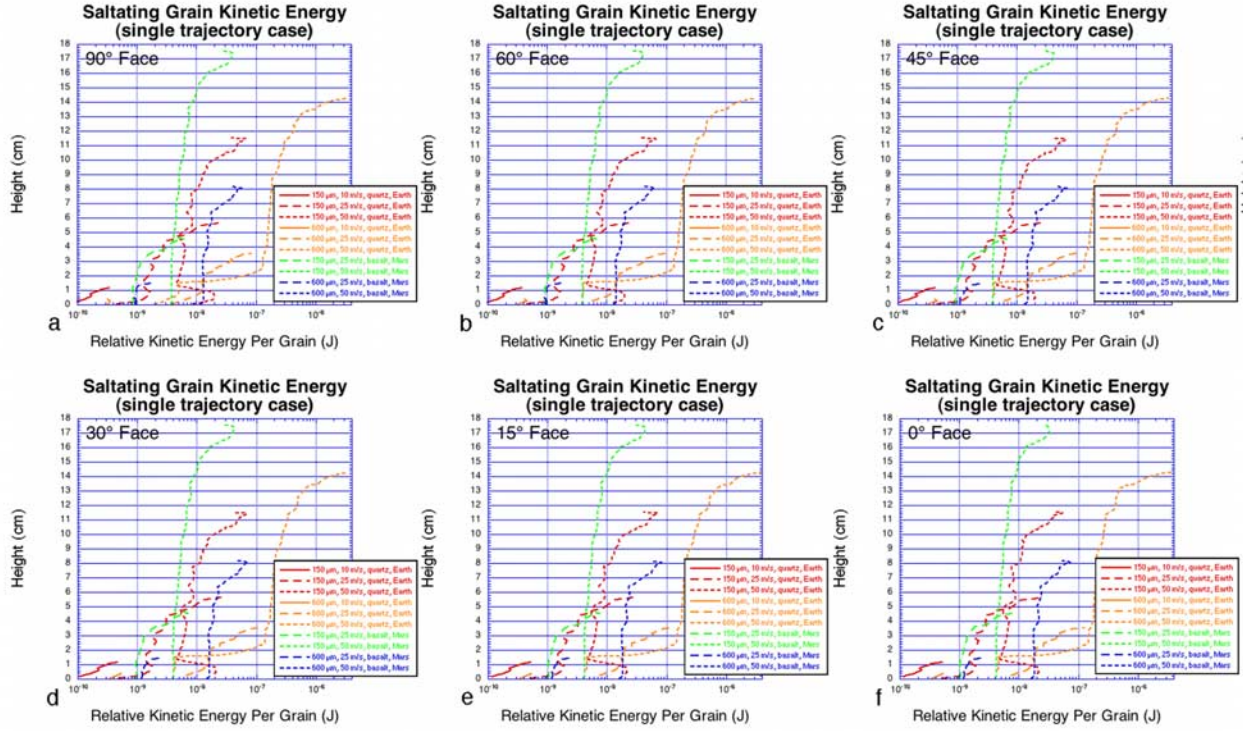


**Figure 13.** Height versus relative kinetic energy per grain for the single trajectory case as seen for a (a) 90° facet, (b) 60° facet, (c) 45° facet, (d) 30° facet, (e) 15° facet, and (f) 0° facet. Kinetic energies are relative values, because they are computed by multiplying the grain kinetic energies at a given height by the fractional concentration predicted at that height.

(maximum  $z$  component along the path) for the velocity terms,

$$P(h_{\max,0}) = \exp(-h_{\max,0}/h_{\max,ave})/h_{\max,ave}, \quad (3)$$

where  $h_{\max,0}$  is the trajectory height of interest and  $h_{\max,ave}$  the mean trajectory height. Here, we took the trajectory heights calculated with the code (Tables 1a and 1b) and substituted this for  $h_{\max,ave}$  and then computed the probability for a range of trajectory heights. The probability density was converted to a normalized probability by multiplying the average  $P(h_{\max})$  within a 1-mm bin by the ratio of bin size to total height range, such that the integral of the normalized probability over the liftoff velocity range was 1. Curves were then smoothed over 9-mm bins to remove artifacts inherent from the saltation code resolution. The results for a 90° face are shown in Figure 16a. The equation balances the probabilities as a function of height, so that saltation conditions in which high trajectories are expected (e.g., 150 μm, 50 m s<sup>-1</sup>, Mars; 600 μm, 50 m s<sup>-1</sup>, Earth) have a greater concentration at large heights compared to low trajectories, whose greatest concentrations are closer to the ground.

[33] The effect of facet angle on the concentration profiles (Figures 16b–16f) was computed in a similar way to the single trajectory case above. The concentrations of ascending grains where  $-\varphi$  was less than  $\theta$  were removed and then the remaining concentrations renormalized. The effects are significant. Because steep ascending trajectories of  $-\varphi < \theta$

are generally in the lower parts of the saltation path, the flux here is reduced, causing the concentration to increase for greater heights. A pronounced kink is seen in several of the profiles, demarcating the height between many removed ascending grains below and a complete mixture of ascending and descending trajectories above.

[34] We now compute the relative kinetic energy for these flux profiles and particle velocities. For each height in the profile, the ascending and descending KEs computed for the single trajectory case were multiplied by their probabilistic fluxes, as computed above, and summed to yield a relative kinetic energy at each height. For heights greater than those computed for the single trajectory case, but predicted by the probabilistic behavior of saltating grains, the KE at the single trajectory apex was multiplied by the normalized concentration. This is somewhat of a simplification in that at any height there will be a mixture of grains of various velocities and kinetic energies, but the relative trends with height and differences among various conditions should be approximately correct. As will be shown below, this is verified in the mass loss versus height experiments.

[35] The relative kinetic energy results are shown in Figure 17. The position of the curves on the  $x$  axis is governed mostly by the kinetic energy, as differences in this parameter among different saltation trajectories for the single trajectory case are an order of magnitude or more (Figure 6) whereas differences in concentration for a given height are much less (Figure 12). Where increases in KE



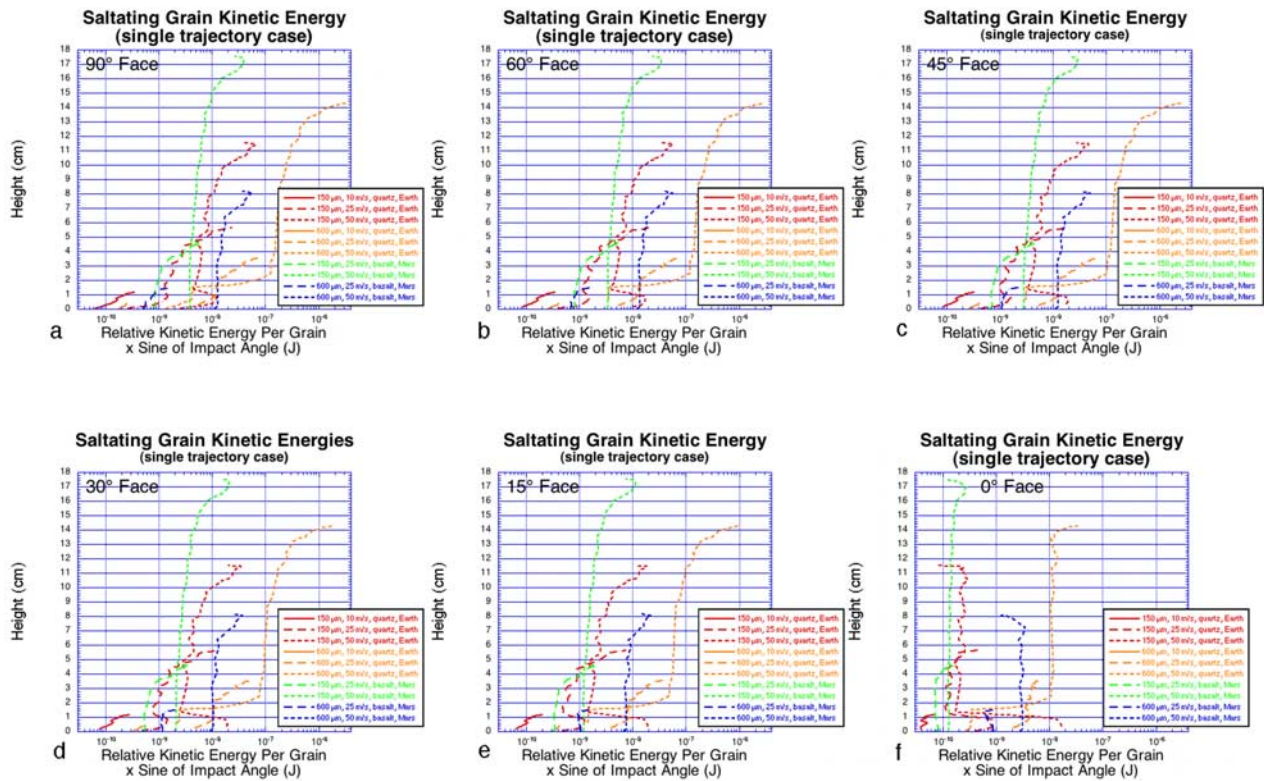


**Figure 14.** Height versus relative kinetic energy per grain multiplied by the sine of the impact angle for the single trajectory case as seen for a (a) 90° facet, (b) 60° facet, (c) 45° facet, (d) 30° facet, (e) 15° facet, and (f) 0° facet. Kinetic energies are relative values, because they are computed by multiplying the grain kinetic energies at a given height by the fractional concentration predicted at that height by the sine of the impact angle.

with height are more significant than decreases in concentration, the curves exhibit a pronounced peak.

[36] The above analysis is incomplete, as it does not compute the kinetic energy transfer of grains onto rock targets. To do this, the effective KEs are multiplied by the sine of the impact angle (Figure 18).

[37] Some observations are derived from these plots:

[38] 1. The kinetic energy and the slope of the rock are anti-correlated. The effect is much more pronounced than the case where only the effect of removing ascending grains is considered (Figure 17).

[39] 2. There is a peak in kinetic energy a few centimeters above the ground for many high KE trajectories and steep angled facets (note that the plots have a logarithmic  $x$  axis to show the range of kinetic energies; a linear plot shows some of the subtle kinks more distinctively). This is due to the low KE of ascending grains or the lack of these grains in the lower parts of the trajectory. Above the kink, the decrease in flux acts to lower the overall energy of the saltation cloud.

[40] 3. The low KE cases and the 150  $\mu\text{m}$ , 50  $\text{m s}^{-1}$  Mars example do not exhibit kinks. For the low KE cases, the particles do not get very high (Figure 6), so that a large fraction of flux is very close to the surface (Figure 16), and the magnitude of KE decrease with height is small compared to most other cases. This results in a decreasing flux with

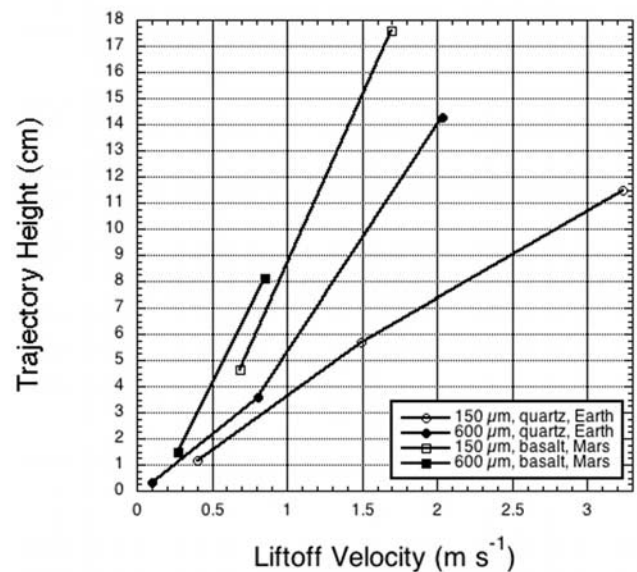


**Figure 15.** Computed trajectory heights versus liftoff velocities for the particle size and planetary conditions used in this paper. Each point in a given curve corresponds to a different 1.2 m wind speed case (10, 25, or 50  $\text{m s}^{-1}$ ).



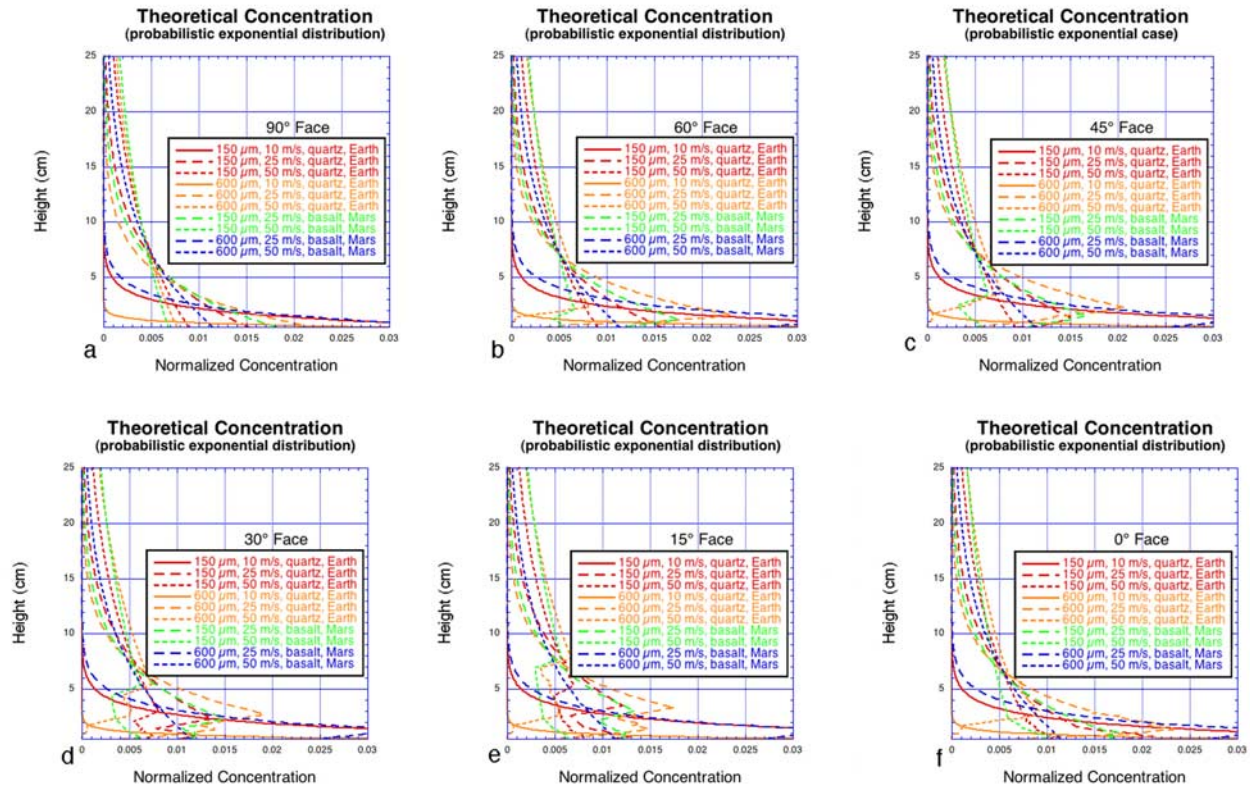


**Figure 16.** Height versus concentration for a probabilistic exponential distribution (after *Anderson and Hallet* [1986]) as seen for a (a) 90° facet, (b) 60° facet, (c) 45° facet, (d) 30° facet, (e) 15° facet, and (f) 0° facet.

height that outweighs the small increasing KE with height. Note that *Anderson* [1986] also computed negligible kinks for saltation cases with low average trajectory heights (see Figure 5 of his paper). In contrast, the 150  $\mu\text{m}$ , 50  $\text{m s}^{-1}$  Mars example has the greatest average trajectory height (Figure 6), such that the change of flux with height is less than that of other modeled cases (Figure 16). When this is multiplied by the KE for a given height (Figure 14), the result is a KE curve with the probabilistic exponential distribution with no discernable kink. This shows that kinks are not apparent in all kinetic energy profiles and their presence is the result of a complex interplay of factors.

[41] 4. The kink heights for 600  $\mu\text{m}$  at the same velocities are slightly greater on Earth than on Mars (3–4 cm compared to 1–2 cm). As will be discussed below, the kink heights found from the numerical models are below that observed in nature.

[42] The reader is urged to treat these plots as approximate representations, not literal reproductions, of what is expected in nature. Natural conditions, with a range of particle sizes and trajectories, are more complex than those modeled here. Therefore these results should be used to gauge relative, but not absolute, differences in kinetic energy with height and between modeled conditions.

### 3.6. Impact Experiments

[43] The results of the impact experiments are shown in Table 2. Most incoming trajectories were flat to slightly

ascending or descending. Particles hitting the 90° face generally were rebounded in the anti-windward direction and then followed an upward trajectory, occasionally hitting again, or went downward and sometimes dropped to the floor. The velocity of the rebounded particles was significantly less than the incoming ones. Because of the 90° face, all particles rebounded in the upwind direction and none in the downwind direction. Five (3.5%) of the 145 tracked particles hit the target two or more times. Most particles hitting the 60° target were deflected upwards and then carried downwind. One particle, out of the 49 tracked, hit twice. Impacts onto the 45° target exhibited more diversity than in the 90°, 60°, and 15° cases. About two thirds of the particles rebounded in the downwind direction. Of these, most hit at a shallow impact angle and rebounded slightly in the downwind direction. A few, comprising 8% of all hits, impacted at very steep impact angles and hit again. All particles hitting the 30° target rebounded in the downwind direction and showed a range of rebound angles similar to the 45° target. Just as in the 45° case, 8% of particles hit the target a second time. All particles hitting the 15° target rebounded in the downwind direction and were deflected at right to obtuse angles relative to the wind.

[44] From these observations, the following is found.

[45] 1. There is an “effective” flux,  $F'$ , due to some particles hitting the target more than once.  $F'$  is always greater than the simple flux,  $F$ , computed from saltation theory.

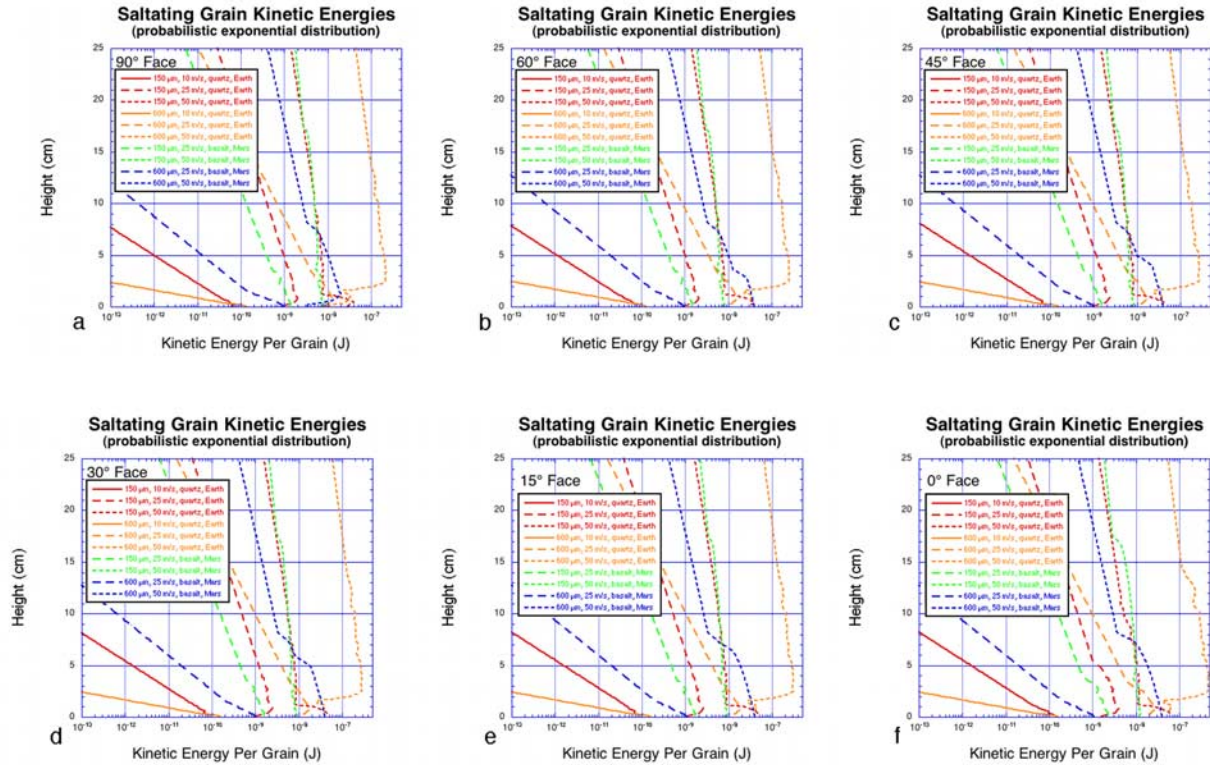


**Figure 17.** Height versus relative kinetic energy per grain for a probabilistic exponential distribution (after *Anderson and Hallet* [1986]) as seen for a (a) 90° facet, (b) 60° facet, (c) 45° facet, (d) 30° facet, (e) 15° facet, and (f) 0° facet. Kinetic energies are relative values, because they are computed by multiplying the grain kinetic energies at a given height by the fractional concentration predicted at that height.

[46] 2. Because trajectories are fairly flat within most parts of the saltation cloud, most impact angles are equal to the facet angle  $\theta$  and rebound at angles close to  $\theta$ , but in the opposite direction (see Figure 7). Relative to horizontal, which can also be considered the wind axis, impact angles are close to  $\theta$  and rebound angles  $2\theta$  (in this case, a rebound angle of 0° is in the downwind direction, 90° is vertical, and 180° is in the upwind direction). Therefore a 90° facet will have particles deflected close to purely upwind, 60° targets slightly upwind, 45° vertical, and facets less than 45° downwind.

[47] 3. The distance traveled on the rebound trajectory for a 90° target will be relatively small because it is pushing against the oncoming wind. This can result in the grain dropping to the ground or re-impacting the target with a low kinetic energy.

[48] 4. Although most grains impacting a 60° target will be rebounded downwind, there is also a significant vertical component. This allows the grains to get higher in the wind profile and, because the sloping 60° target is farther away at greater heights of the rebound trajectory, any subsequent impacts will have greater kinetic energy than in the 90° target rebound case.

[49] 5. For 45° targets, the particles will be deflected vertically, potentially reaching heights in the boundary layer

greater than if they were not bounced upward at all, such that their acceleration downwind will be significant. If they impact, they will have a KE proportional to the amount of downwind distance traveled, their height in the velocity profile, and the impact angle.

[50] 6. Grains impacting targets less than 45° will be mostly or entirely accelerated downwind. The kinetic energy of rebounded grains can be high, but their actual kinetic energy transfer to the rock may be low because of the shallow impact angles. Also, because the horizontal distance between impacts is greater for a shallow slope compared to an intermediate one, the chances of a single rock face being hit by the same sand grain more than once is proportional to slope angle.

[51] 7. Considering all of the above, it seems that the effect of rebound will exert the greatest effect for intermediate slopes.

[52] The results of the impact experiments indicate that the degree of abrasion on intermediate slopes should be greater than that computed from the simple saltation calculations described previously. How much this counteracts the effect of reduced kinetic energy due to non-perpendicular collisions relative to 90° targets cannot be quantified without more detailed numerical modeling. At present, we recognize this as a possibly significant effect to consider



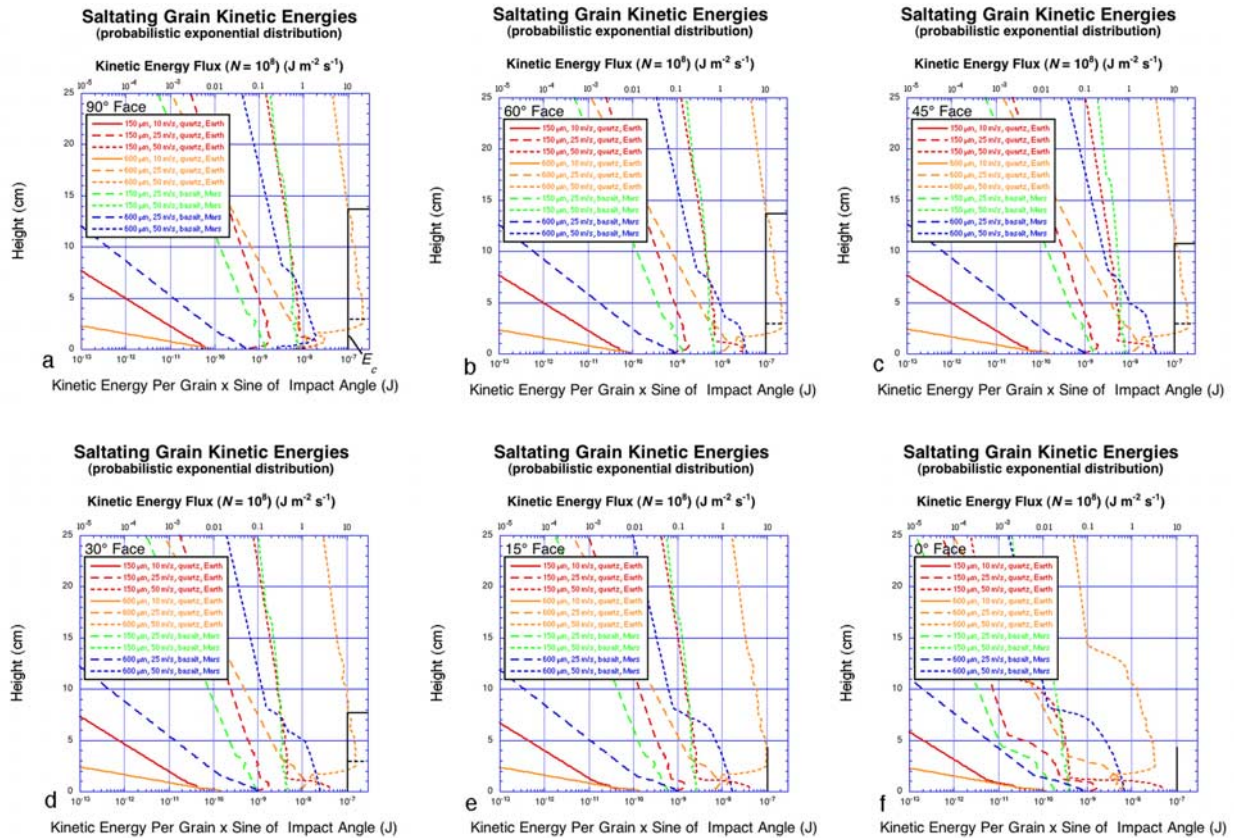


**Figure 18.** Height versus relative kinetic energy per grain multiplied by the sine of the impact angle for a probabilistic exponential distribution (after *Anderson and Hallet* [1986]) as seen for a (a) 90° facet, (b) 60° facet, (c) 45° facet, (d) 30° facet, (e) 15° facet, and (f) 0° facet. Kinetic energies are relative values, because they are computed by multiplying the grain kinetic energies at a given height by the fractional concentration predicted at that height by the sine of the impact angle. The top of each graph shows values for kinetic energy flux, as discussed in the text. The vertical line, labeled as “ $E_C$ ” in Figure 18a, is a hypothetical critical kinetic energy above which abrasion occurs, so that where curves are to the right of the line, abrasion is predicted for the  $E_C$  modeled. The dotted horizontal line is placed at 3 cm and demarcates the height at which abrasion is discussed in the text. The solid horizontal line shows the maximum height of abrasion for 90°, 60°, 45°, and 30° facet angles.

in the interpretation of field data, spacecraft images, and laboratory studies of ventifacts.

### 3.7. Comparison to Abrasion Experiments

[53] Here we examine abrasion as a function of the interdependent effects of target angle, height, and kinetic energy observed in the wind tunnel and compare the results to the above predictions.

#### 3.7.1. Abrasion as a Function of Target Angle

[54] The theoretical work described in sections 3.1–3.5 indicates that the degree of abrasion should correlate to facet angle. This is verified experimentally by comparing mass loss for different angled targets under low wind velocity ( $11 \text{ m s}^{-1}$ ) terrestrial conditions in the wind tunnel (Figure 19a; note that another version of this plot is printed in color in the work by *Bridges et al.* [2004]). Although there is some scatter in the data, families of points corresponding to distinct facet angles are apparent,

with the facet angle generally corresponding to the mass loss. The 90°, 60°, and 45° families are more closely clustered than the 30° and 15° groups. This may be attributable to more efficient abrasion at the higher angles, as the sine of the angle quickly drops off at low angles. The size of targets (5 cm long along the dip slope) were insufficient to judge the effects of ascending/descending flux and rebound as a function of angle that were discussed in previous sections.

[55] The targets abraded under Martian conditions show a much more scattered distribution of points, although the greatest mass loss is recorded in steep (60–90°) targets and the least in shallow (15–30°) targets (Figure 19b). A likely explanation for this is that kinetic energy of grains at  $11 \text{ m s}^{-1}$  is much closer to  $E_C$  than grains moving faster, so that abrasion potential at shallow facet angles is more effectively reduced at the slower speeds characteristic of terrestrial saltation compared to the higher speeds



**Table 2.** Observations of Wind Tunnel Target Impacts<sup>a</sup>

Target	<i>N</i>	<i>N</i> , Typical Trajectory/One Impact	<i>N</i> , Two Impacts	<i>N</i> , Three Impacts	Atypical
90°	145	101 (69.7%) impacts front, then deflected straight out; then follows upward trajectory	4 (2.8%)	1 (0.7%) 3rd impacts on top	39 (26.9%) Side or erratic.
60°	49	48 (98%) impacts and then deflected straight up	1 (2%)		
45°	103	94 (91%)  28 (30%) impacts at steep angle and high speed; rebounds slightly opposite to wind direction 2 (2%) impacts at steep angle and slow to medium speed; rebounds opposite to wind direction but blown back over top 52 (55%) impacts at shallow angle at medium speed and rebounds slightly in + wind direction 12 (13%) impacts at very shallow angles and low speeds; rebounds at shallow angles and carried just above surface	8 (8%) impacts at steep angle, low speed	1 (1%) impacts at very low speed and shallow angle	
30°	36	33 (92%)  16 (48%) impacts at shallower (relative to below) angles and low to medium speed; rebounds into + wind direction 12 (36%) impacts at steeper (relative to above) angle and high speed; rebounds at high angles in + wind direction and passes over the top. 3 (9%) impacts at shallow angles and low speeds. Rolls or bounces before being lift up. 2 (6%) lift in front of target in – wind direction, then change direction and impacts target near top before passing over	3 (8%) impacts at steep angle and low speed		
15°	20	20 (100%) particles impact near the bottom and shoot up; those on the upper face rebound at obtuse angles			

<sup>a</sup>*N* is the number of observed particles per category. Subcategory percentages are relative to category.

predicted for Martian saltation (see further discussion below).

### 3.7.2. Abrasion Rate as a Function of Height

[56] Abrasion of targets in the wind tunnel at 20, 40, and 60 cm shows a clear decrease with height (Figure 20). Target mass loss to sand expended is inversely proportional to height, so that for greater amounts of abrasion time (measured here as amount of hopper sand used), variation in mass loss with height decreases. Note that these heights are above the kink region, so that mass loss is expected to decrease with height as shown. The rate of decrease with height may seem less than that predicted by the relative kinetic energy curves in Figure 18. This is probably because sand that was dropped from the hopper and subsequently bounced downwind increased the flux tens of centimeters above the wind tunnel floor compared to the flux expected from saltation at the surface, and the low critical KE value for the sandstone simulant targets.

### 3.7.3. Abrasion Rate as a Function of Kinetic Energy

[57] Mass loss as a function of target angle for various wind speeds (kinetic energy) is shown in Figure 19. There are several observations. (1) Experiments for wind speeds ranging from 35 to 58 m s<sup>−1</sup> at Mars pressure exhibit a greater mass loss than at 11 m s<sup>−1</sup> under Earth pressure for steep to intermediate (90 to 45°) target angles, with the

amount of difference proportional to angle. (2) For shallow (30° and less) target angles, the mass loss differences between the high and low kinetic energy cases are negligible. (3) For 35 and 52–58 m s<sup>−1</sup> at Mars pressure, there is no consistent difference in mass loss between the two sets of experiments.

[58] These observations are consistent with the previous theoretical analysis. The particle velocities in these experiments are not known, but we can assume that they are greater in a 35–58 m s<sup>−1</sup> low pressure wind compared to an 11 m s<sup>−1</sup> high-pressure wind. (However, note that wind velocities do not correlate to the particle velocities and thereby the kinetic energies. Particle entrainment by the wind is much more efficient at terrestrial compared to Martian pressures [Greeley *et al.*, 1983] (Figure 5b).) There is some value of kinetic energy below which the targets do not abrade significantly ( $E_C$ ). The difference in kinetic energies for two velocities  $v_1$  and  $v_2$  is  $[v_1^2 - v_2^2]\sin\theta$ , such that there is only half the difference at 30° and about a quarter the difference at 15° compared to the difference at 90°. Therefore the experiments and this simple theoretical treatment show that kinetic energy differences most strongly affect steep targets or high impact angles, with the differences at small angles being small enough not to have a significant effect on mass loss.

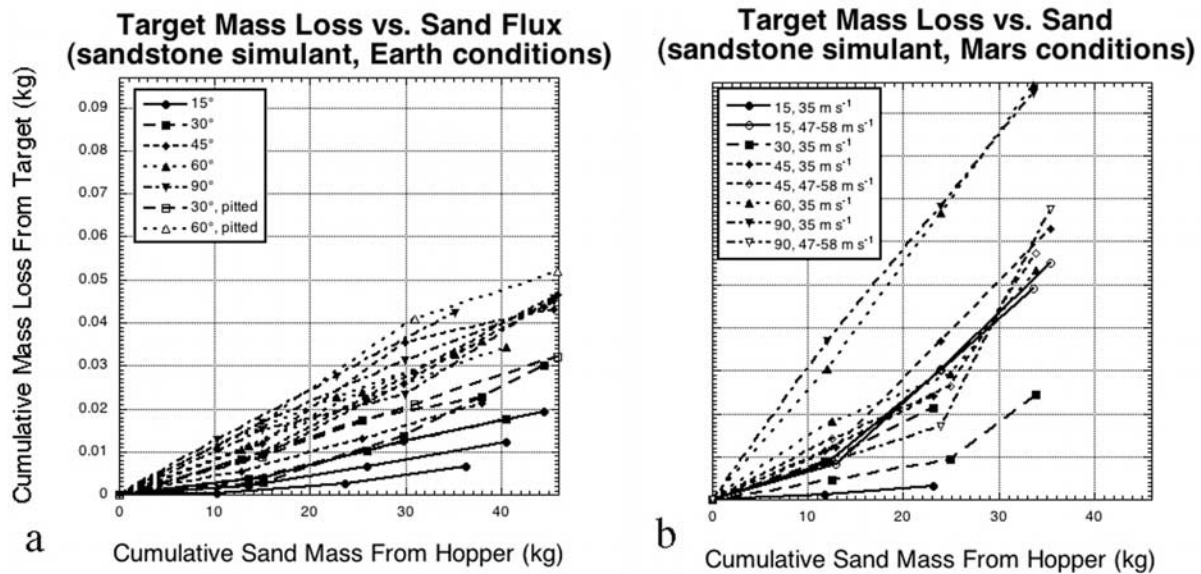


**Figure 19.** (a) Cumulative mass loss from sandstone simulant targets versus sand mass expended from the wind tunnel hopper. All runs were conducted at Earth pressure ( $\sim 1$  bar) with a freestream wind speed of  $\sim 11 \text{ m s}^{-1}$ . Listed angles indicate the slope of the front face of the target relative to the oncoming wind. One  $30^\circ$  and one  $60^\circ$  target were etched with pits prior to abrasion and showed enhanced mass loss. Plotted points indicate mass loss measurements following each experiment, with lines connecting the points for an individual target. (b) Cumulative mass loss from sandstone simulant targets versus sand mass expended from the wind tunnel hopper conducted at Mars pressure ( $\sim 10$  mb) conditions for the freestream wind speeds shown.

[59] The lack of differences between the 35 and 47–58  $\text{m s}^{-1}$  (Mars pressure) results relative to the differences between these two sets of experiments and 11  $\text{m s}^{-1}$  (Earth pressure) results are due to different relative kinetic energies. Assuming that the particle velocity is proportional to that of the wind, the ratio of KEs for 35 to 11  $\text{m s}^{-1}$  is 5.2 whereas it is 2.3 for 51.5 to 35  $\text{m s}^{-1}$ . In fact, the difference in the ratios may even be greater, given the low particle speed to wind speed ratio computed for terrestrial sand at 10  $\text{m s}^{-1}$  (Figure 5b). We also speculate that given the weakness of these targets, there may be a value at which maximum abrasion efficiency is reached and beyond which the effects of further kinetic energy increase is negligible. This value is unlikely to get reached for crystalline rocks in nature.

## 4. Discussion

### 4.1. Kinetic Energy Heights

[60] The height over which apparent sand abrasion occurs in the field is from the surface up to about a meter [Laity, 1987]. Previous field and theoretical studies have also measured abrasion maxima, with the field studies [Sharp, 1964, 1980; Wilshire *et al.*, 1981] indicating heights of about 10–25 cm, a factor of 3 or more greater than those reported here. Even greater heights, up to 43 cm, have been observed downwind of roads [Wilshire *et al.*, 1981]. In contrast, the previous theoretical work of Anderson [1986] computed kinetic energy maxima (albeit for different particle sizes and friction speeds), closer to those reported here ( $\sim 2$ –10 cm), but still in the lower bounds of the field measurements. In a wind tunnel study of abrasion height,

Liu *et al.* [2003] found maximum abrasion 5–12.5 cm above the surface, with the value proportional to wind speed over a range of 10–22  $\text{m s}^{-1}$ . The work of Liu *et al.* [2003], and the results reported here, are constrained by the limited fetch of a wind tunnel, which cannot completely simulate the multiple saltation rebounds and impact-induced saltation (Liu *et al.* report that the “working section” of their wind tunnel was 16.2 m long; the distance between the hopper and targets in our experiments was 4 m). Suzuki and Takahashi [1981] computed a maximum abrasion height of  $\sim 30$  cm; however, they assumed that the sand grains travel at the same velocity as the wind, which is only appropriate for suspended, not saltated, grains.

[61] The maximum kinetic energy heights reported here and by Anderson [1986] have not incorporated the effects of rebound from a hard or granular surface. In addition, we have not directly modeled the impact threshold case where saltating particles liberate others in the bed (however, as discussed above, the limited experimental results for liftoff velocities for impact-induced saltation [White and Schulz, 1977] are similar to those predicted here, allowing us to fit our results to the equations predicted for this case). Therefore our curves should be considered lower bounds on the height axis and might be moved upward for considering more field-like cases. However, the shape of the curves and the relative differences between them should be approximately correct.

### 4.2. Implications for Rock Morphologic Evolution

[62] For simplicity, consider a rock prior to abrasion that has a facet oriented  $90^\circ$  to the wind flow. Let us also

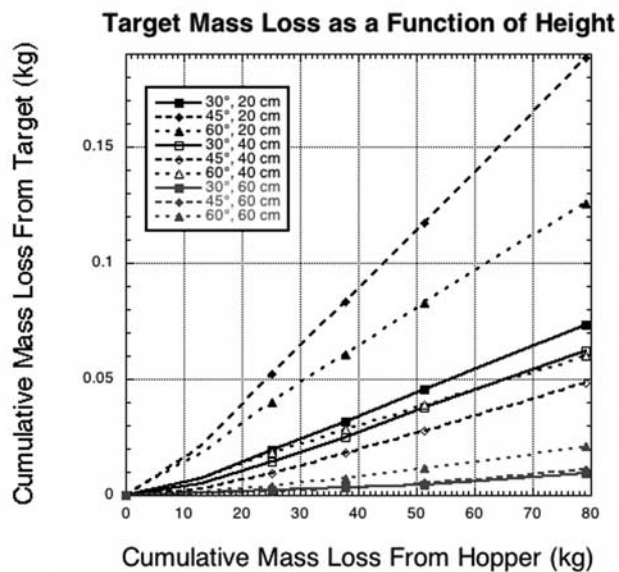


**Figure 20.** Cumulative mass loss from sandstone simulant targets versus sand mass expended from the wind tunnel hopper for three heights. All runs were conducted at Earth pressure ( $\sim 1$  bar) with a freestream wind speed of  $\sim 11 \text{ m s}^{-1}$ . Plotted points indicate mass loss measurements following each experiment, with lines connecting the points for an individual target.

imagine a critical kinetic energy ( $E_C$ ) of  $1 \times 10^{-7} \text{ J}$ , below which abrasion is negligible, such that shape and texture changes are barely noticeable on a geologic timescale (Figure 18). We will consider abrasion by  $600 \mu\text{m}$  sand at  $50 \text{ m s}^{-1}$  on Earth. The rock is of sufficient size such that it is exposed to saltating grains above the height of peak kinetic energy ( $\sim 3 \text{ cm}$ ) and, of course, to all saltating grains at heights below. Finally, we will assume that the abrasion environment is such that the impact kinetic energies for the initial rock shape are above  $E_C$  for all heights. The point at which  $E_C$  is reached will depend on the facet slope, abrading environment, and rock type. In terms of Figure 18, this can be parameterized as where the curve of relative KE versus height plots against the vertical line defining  $E_C$ . However, a single curve cannot effectively define the evolution of a facet because the slope of that facet changes as it is abraded. Rather, the following general evolution is proposed, in this case considering a rock facet originally oriented  $90^\circ$  to horizontal.

[63] 1. The rock facet, initially angled  $90^\circ$ , will retreat as it is abraded away, with the rate of abrasion greater in the upper ( $\sim 3 \text{ cm}$ ) region where kinetic energy is higher. This will result in the upper part of the rock sloping back, with the amount of slope proportional to the kinetic energy at that height. The kinetic energy on the bottom part of the rock will be lower, such that the slope change from  $90^\circ$  is much less than higher up.

[64] 2. The upper part of the rock continues to abrade, but at a decreasing rate because of the lower impact angles resulting from the reduced slope. At the same time, the lower part of the rock continues to abrade at about the same relatively low rate as in step 1 because its slope has not changed significantly.

[65] 3. Eventually, the kinetic energy at a given height reaches the critical KE at which further change is negligible. In the case illustrated in Figure 18, the height range over which abrasion occurs shrinks with decreasing facet angle because the KE curve, with its distinctive maximum, moves to the left. In the upper part of the rock surface, significant abrasion ceases when the slope is such that the KE of the impacting grains ( $E_G$ ) is below the critical value. In the lower part of the rock surface, the angle at which this occurs will be steeper than that for the upper part of the rock, as kinetic energies were lower to begin with and therefore fall below  $E_C$  at greater slopes.

[66] Rocks of heights greater than where  $E_C$  is reached will develop a notch at the maximum kinetic energy height, with abrasion ceasing first at heights above and below this.

[67] Differential erosion as a function of height to form facets has been proposed previously from experimental and field work. Sharp [1948] hypothesized that rocks with tops above the zone of maximum abrasion developed initially concave profiles that eventually flattened to an inclined slope. He noted that wind cut facets in his field study area (Big Horn Mountains, Wyoming) were generally greater than  $20\text{--}30^\circ$  and he proposed that abrasion effectively ceased at shallower angles. This was consistent with even earlier studies suggesting a reduction in abrasion at angles less than  $20\text{--}30^\circ$  [Woodworth, 1894; Bryan, 1931; Schoewe, 1932; Needham, 1937]. The scenario here adds to the contributions of these earlier studies by modeling the process using numerical saltation calculations and considering heights both below and above the zone of maximum abrasion.

#### 4.3. Conversion to Kinetic Energy Flux

[68] The kinetic energy values in the previous plots are scaled by a probability distribution, as described above. To compute a kinetic energy flux (energy per area per time [ $\text{J m}^{-2} \text{s}^{-1}$ ]) one must assume or estimate the number ( $N$ ) of grains passing through a unit area per unit time. This depends on bed mobility, fetch (i.e., the length scale over which impact saltation can liberate more particles to participate in saltation downwind), and other factors. We compare two previous papers, one theoretical, the other experimental. In numerical simulations of saltation for single and multiple trajectories under terrestrial conditions, Anderson [1986] computed  $N$  values of  $1.6 \times 10^6$  (single saltation trajectory model) and  $4.7 \times 10^5 \text{ m}^{-2} \text{s}^{-1}$  (multiple saltation trajectory model), yielding kinetic energy fluxes at the KE peak of  $\sim 25$  and  $6.5 \text{ J m}^{-2} \text{s}^{-1}$ , respectively. Multiplying the values of  $N$  used by Anderson [1986] by the appropriate KE curves in this paper (Figures 13a and 17a, respectively; note that Anderson [1986] did not consider the effects of impact angle on KE as showed in Figures 14 and 18) gives kinetic energy fluxes about 3–4 orders of magnitude less than he obtained. In contrast, White [1982] found that the flux measured in the wind tunnel for  $92\text{-}\mu\text{m}$  quartz particles,  $10 \text{ cm}$  above the surface at freestream velocities of  $10\text{--}11 \text{ m s}^{-1}$  were on the order of  $0.1 \text{ kg m}^{-2} \text{s}^{-1}$ . A  $92\text{-}\mu\text{m}$  quartz particle has a mass of about  $10^{-9} \text{ kg}$ , yielding  $N = 10^8 \text{ m}^{-2} \text{s}^{-1}$ . Assuming particle velocities ranging from  $1$  to  $10 \text{ m s}^{-1}$  ( $\sim 0.1\text{--}1 \times$  freestream)



yields a kinetic energy flux of  $0.05\text{--}5\text{ J m}^{-2}\text{ s}^{-1}$ . Multiplying the KE curves in this paper by  $N = 10^8\text{ m}^{-2}\text{ s}^{-1}$  gives kinetic energy fluxes closer to those derived from the White [1982] data. The discrepancy between the two published results could be because the numerical methods of Anderson [1986] summed the contributions of all predicted trajectories, including high velocity ones that will have a greater contribution to the kinetic energy flux even if their fraction of total trajectories is small. More wind tunnel and field experiments of kinetic energy flux for a range of conditions are clearly needed. For now, if the reader wishes to convert the curves into kinetic energy flux space, multiplying the bottom  $x$  axis values by  $\sim 10^8\text{ m}^{-2}\text{ s}^{-1}$  may be approximately correct to within an order of magnitude if the bed is fairly mobile as in the White [1982] experiments (Figure 18, top  $x$  axis).

#### 4.4. Implications for Abrasion Rates

[69] Ultimately, we would like to know the amount of material removed from a rock surface given the incoming kinetic energy. Experimental abrasion studies show that the mass of removed material is proportional to incoming particle kinetic energy [Suzuki and Takahashi, 1981; Greeley et al., 1982]. Values of abrasion susceptibility for basalt, probably the most abundant rock type on Mars and a common variety in terrestrial abrasion settings, range from  $\sim 10^{-10}$  to  $\sim 10^{-8}$  for 125- to 180- $\mu\text{m}$  quartz grains at a velocity of  $\sim 10\text{--}50\text{ m s}^{-1}$  [Greeley et al., 1982]. Assuming  $N = 10^8$  and a mass of  $5 \times 10^{-9}\text{ kg}$  for a 150- $\mu\text{m}$  quartz grain, yields rock abrasion rates of  $5 \times 10^{-11}$  to  $5 \times 10^{-9}\text{ kg s}^{-1}$ . This translates to about 7–700 Earth years to abrade 1 kg of basalt, assuming constant abrasion. Noting that kinetic energy in our analysis and plots (Figure 18) is approximately proportional to the sine of the target angle, KE for  $30^\circ$  and  $15^\circ$  target angles is predicted as about one half and one quarter of that compared to a  $90^\circ$  face. This is in agreement with some previous theoretical and experimental work examining the abrasion of silicon crystals [Routbort et al., 1980; Scattergood and Routbort, 1983]. By comparison, Greeley et al. [1982] found a relationship of basalt  $S_a$  that is proportional to the sine of the impact (target) angle down to  $30^\circ$ , below which the susceptibility was observed to increase significantly. This is in contrast to the results here and other previous research [Woodworth, 1894; Bryan, 1931; Schoewe, 1932; Needham, 1937; Sharp, 1948]. Greeley et al. [1982] attributed their results to a cutting and gouging mechanism whereby shallow impacts affect a greater surface area than more perpendicular collisions, a process not considered in our model. Considering the results of Greeley et al. [1982], basalt abrasion rate will decrease as the angle of the rock face decreases from initially high values down to  $\sim 30^\circ$ . If abrasion continues to proceed such that the rock face is abraded to angles shallower than  $30^\circ$ , abrasion could increase, further eroding the rock. The uncertainties in the abrasion mechanism at low angles points to the need for further research in this area.

#### 4.5. Comparison of Analyses to Terrestrial and Martian Ventifacts

[70] The above analyses lead to several predictions about ventifacts. The first is that original rock shape,

approximated here by facet angle relative to the oncoming wind, exerts a strong effect on abrasion rate. Environments in which the effective KE versus height curves are right at or below the critical KE line should experience little or no abrasion. This includes conditions just above threshold where the kinetic energy of impacts is insufficient. On Earth this is seen where low velocity winds blow, yet ventifacts with elongated pits, flutes, and grooves in those wind directions are not found [Laity, 1987, 1992, 1995; Bridges et al., 2004].

[71] Environments in which the effective KE versus height curves are slightly above the critical KE line should only experience abrasion at heights near the kink region and only for steep rock angles. The result should be abraded rocks with windward faces consisting of a steep face at their base and upper faces with intermediate to slightly steep angles. Environments in which the relative KE versus height curves are significantly greater than the critical KE line should experience abrasion at most or all heights in the saltation cloud for (1) steep rock angles or (2) given sufficient energy, for all angles. In case 1, this should result in rocks with a sloping lower face above which is a ramp of even greater slope. In case 2, rocks will only be preserved if saltation ceases. If this occurs early enough, the rocks should be preserved with similar characteristics to those in case 1. If abrasion occurs over a longer interval, a single facet angle will develop, with the angle of the facet decreasing over time. This is verified in field experiments by Sharp [1964], over a period of 11 years, using bricks and hydrocal blocks that show a base of uneroded material below an abraded region. Some rocks on Earth [Laity, 1994] and Mars [Bridges et al., 1999; Greeley et al., 2002] also exhibit these characteristics. The wind tunnel experiments of Bridges et al. [2004] document this phenomena as well, although no correlation with target angle was recorded. A definitive correlation between initial facet angle and the limited abrasion at the base of a rock, and the dependence of this on critical KE, hence allowing a discrimination between modes where the KE versus height curves are slightly as opposed to significantly greater than  $E_C$ , has not yet been explored.

[72] Our results also predict that rocks of sufficient height above the kink region will exhibit a notch at the kink and possibly a pedestal shape characterized by a lack of abrasion above the saltation cloud. This is consistent with field evidence indicating that abrasion rarely occurs at heights greater than 1 m [Laity, 1987]. Rocks of this size or taller in highly abrasive environments, such as Antarctica, commonly exhibit notched and pedestal shapes [Greeley and Iversen, 1985; Laity, 1987].

[73] Intermediate-sloping rock faces of sufficient size can be abraded at greater heights above the ground compared to steep faces. This is because rebounded grains are bounced approximately vertically into the wind profile, where high speed winds accelerate them downwind, to perhaps rebound against the rock again. This should result in intermediate- to shallow-sloping outcrops (as opposed to small float) getting abraded at greater heights than steep outcrops. To the authors' knowledge, a direct observation of this has not been made. However, a related phenomenon is the elevated heights of abrasion that have been recorded for saltation on

road pavement relative to that seen adjacent to a sand surface [Wilshire *et al.*, 1981; Laity, 1994]. The pavement example shows that fairly elastic collisions in which the wind is allowed to move particles downwind with sufficient kinetic energy can enhance abrasion as a function of height. Just as particles can saltate multiple times over a hard road, so should they be able to impact an intermediate dipping rock more than once, increasing the effective flux on that surface.

[74] It is not easy to make general statements about the abrasion differences on Earth and Mars, as on each planet there can be differences in wind speeds and particle size which affect the kinetic energy and trajectories of saltating grains. However, by constraining these parameters, some inferences can be made. First, the particle size moved at the minimum threshold friction speed on Earth and Mars is close to 100  $\mu\text{m}$  [Greeley *et al.*, 1976; Iversen and White, 1982] and, indeed, fine to medium sand ( $\sim 125\text{--}250\ \mu\text{m}$ ) is the most common grain size for dunes and aeolian sandstones on Earth [Bagnold, 1941; Ahlbrandt, 1979; McKee, 1979]. In this case, kinetic energies are about the same for 50  $\text{m s}^{-1}$  winds and  $\sim 2\text{--}5\times$  greater on Earth for 25  $\text{m s}^{-1}$  winds. Second, minimum threshold friction speeds are about 0.02 and 0.2  $\text{m s}^{-1}$  on Earth and Mars respectively [Greeley *et al.*, 1982]. Under these conditions, kinetic energies are greater on Mars by about an order of magnitude. On Earth, comparison of ventifact orientation to free stream wind speed at heights of 0.5–3 m shows the best alignment with the highest speed winds [Laity, 1987, 1995; J. E. Laity, personal communication, 2005]. In a recent study, a better alignment for 3-m-high winds  $>10\ \text{m s}^{-1}$  (near threshold) than for winds  $>5\ \text{m s}^{-1}$ , was found, indicating that abrasion occurs at some value above, not at, 10  $\text{m s}^{-1}$  [Bridges *et al.*, 2004]. At threshold conditions on Mars, sand will be saltated at much higher kinetic energies than at threshold on Earth and should be much more effective at forming ventifacts. In other words, at threshold, abrasion is virtually certain on Mars and may occur on Earth.

[75] This implies that shorter duration events on Mars compared to those on Earth can accomplish equivalent amounts of abrasion. Similar arguments for raising dust by winds, that is, conditions that are rare yet powerful, have been suggested for nearly 30 years [Pollack *et al.*, 1976]. It has also been noted that abrasion of sand from hitting rocks (as opposed to the reverse which is of concern in this paper) will be more potent on Mars because of the greater threshold friction speeds there [Krinsley *et al.*, 1979]. The fact that threshold conditions on Mars produce high KE saltation, but that not all rocks are eroded to a common geometry, argues for abrasion being a very ephemeral process on the planet. As such, the presence of ventifacts on Mars [Bridges *et al.*, 1999; Greeley *et al.*, 2004] is not necessarily attributable to past climate regimes when conditions could have been more conducive to winds above threshold. In the current environment, such winds are reached infrequently but, when they are, can be quite effective at accelerating sand to high kinetic energy. Sand supply is also a factor. On Mars today, dunes are commonly trapped in craters and other topographic lows [Breed *et al.*, 1979; Malin *et al.*, 1998; Thomas *et al.*, 1999], such that they can no longer be easily transported across the surface.

Therefore the quantity of sand that is potentially available for abrasion in most areas is less today than in the past. A more thorough resolution of this question requires further modeling and study, as well as better near-surface wind measurements on Mars.

[76] We can also consider the size of sand found on Mars and whether this is likely to have participated in abrasion. Results from the *Spirit* MER rover show a range of sizes from fine to coarse sand, including ripples with characteristic coarser materials at their crests [Greeley *et al.*, 2004; Herkenhoff *et al.*, 2004]. As of this writing, neither rover has analyzed unequivocal dune material. Orbital thermal inertia measurements of Martian dunes indicate sand particle sizes on the order of  $500 \pm 100\ \mu\text{m}$  [Edgett and Christensen, 1991]. Results in this paper show that, for near surface winds of 25  $\text{m s}^{-1}$ , if sand near 600  $\mu\text{m}$  size on Mars is the abrasive agent, its abrasion potential is about half that of 150- $\mu\text{m}$  Mars sand, but still greater than terrestrial fine sand at the same wind speed. Therefore, if winds are sufficient, a large range of particle sizes on Mars can cause abrasion and at a greater rate than on Earth.

## 5. Conclusions

[77] We have computed relative kinetic energies for different types of saltation conditions under terrestrial and Martian conditions. Results show that the abrasion potential can vary significantly as a function of wind speed and particle size. Profiles of height versus integrated kinetic energy for high KE conditions and steep targets generally exhibit a pronounced kink above the surface where the optimum balance of particle concentration and kinetic energy occur. Kink heights are roughly equivalent on Earth and Mars, with slightly higher values on Earth for 600- $\mu\text{m}$  sand. Rocks should abrade most in this region and less so at higher and lower elevations, and, as such, show an evolution in shape as a function of time. Rocks with heights near the kink region will abrade at a greater rate higher up until adjustments in the angle of the face cause more symmetric abrasion about most of the rock face. This will lead to an evolution of steep rock faces in abrading environments from initially orthogonal to the wind to a form marked by a lower steep face and upper face that is sloped backward or, given sufficient abrasion, a more or less single ramped facet. The ability for particles to have high kinetic energy multiple rebounds has been observed in wind tunnel tests, but the effect is not well quantified. It is likely to enhance abrasion for intermediately sloping rock faces. We expect that the physics of abrasion is relatively similar on Earth and Mars, but the higher threshold conditions in the thin Mars atmosphere means that when abrasion does occur, it is consistently a high kinetic energy process.

[78] **Acknowledgments.** This paper benefited from detailed reviews by two anonymous reviewers. We are indebted to UC Davis students J. A. Byron and S. N. D'Souza who painstakingly analyzed the high speed video data of particle collisions. Many conversations and field work with J. E. Laity significantly improved this paper. M. P. Golombek provided useful comments on the manuscript. Support by NASA to the MARSWIT facility is gratefully acknowledged. This research was supported by a grant from the Planetary Geology and Geophysics Program. The research in this paper



was carried out at the Jet Propulsion Laboratory, California Institute of Technology, under a contract with the National Aeronautics and Space Administration.

## References

- Ahlbrandt, T. S. (1979), Textural parameters of eolian deposits, in *A Study of Global Sand Seas*, edited by E. D. McKee, *U.S. Geol. Surv. Prof. Pap.*, 1052, 21–51.
- Anderson, R. S. (1986), Erosion profiles due to particles entrained by wind: Application of an eolian sediment-transport model, *Geol. Soc. Am. Bull.*, 97, 1270–1278.
- Anderson, R. S., and B. Hallet (1986), Sediment transport by wind: Toward a general model, *Geol. Soc. Am. Bull.*, 97, 523–535.
- Bagnold, R. A. (1941), *The Physics of Blown Sand and Desert Dunes*, Methuen, New York.
- Bagnold, R. A. (1973), The nature of saltation and of 'bedload' transport in water, *Proc. R. Soc. London, Ser. A*, 332, 473–504.
- Binder, A. B., R. E. Arvidson, E. A. Guinness, K. L. Jones, E. C. Morris, T. A. Mutch, D. C. Pieri, and C. Sagan (1977), The geology of the Viking Lander 1 site, *J. Geophys. Res.*, 82, 4439–4451.
- Breed, C. S., M. J. Grolrier, and J. F. McCauley (1979), Morphology and distribution of common "sand" dunes on Mars: Comparison to Earth, *J. Geophys. Res.*, 84, 8183–8204.
- Bridges, N. T., R. Greeley, A. F. C. Haldemann, K. E. Herkenhoff, M. Kraft, T. J. Parker, and A. W. Ward (1999), Ventifacts at the Pathfinder landing site, *J. Geophys. Res.*, 104, 8595–8615.
- Bridges, N. T., J. E. Laity, R. Greeley, J. Phoreman, and E. E. Eddlemon (2004), Mechanisms of rock abrasion and ventifact formation from laboratory and field analog studies with applications to Mars, *Planet. Space Sci.*, 52, 199–213.
- Bryan, K. (1931), Wind-worn stones or ventifacts—A discussion and bibliography: Committee on Sedimentation, 1929–30, in *National Research Council Circular* 98, pp. 29–50, Natl. Acad. Press, Washington, D. C.
- Chepil, W. S. (1958), The use of evenly spaced hemispheres to evaluate aerodynamic forces on a soil surface, *Eos Trans. AGU*, 39, 397–403.
- Chepil, W. S. (1959), Equilibrium of soil grains at the threshold of movement by wind, *Soil Sci. Soc. Am. Proc.*, 1959, 422–428.
- Christensen, P. R., et al. (2004), Mineralogy at Meridiani Planum from the Mini-TES Experiment on the Opportunity Rover, *Science*, 306, 1733–1739.
- Edgett, K. S., and P. R. Christensen (1991), The particle size of Martian aeolian dunes, *J. Geophys. Res.*, 96, 22,765–22,776.
- Edgett, K. S., and M. C. Malin (2000), New views of Mars eolian activity, materials, and surface properties: Three vignettes from the Mars Global Surveyor Mars Orbiter Camera, *J. Geophys. Res.*, 105, 1623–1650.
- Einstein, H. A., and E. El-Samni (1949), Hydrodynamic forces on a rough wall, *Rev. Mod. Phys.*, 21, 520–524.
- Francis, J. R. D. (1973), Experiments on the motion of solitary grains along the bed of a water-stream, *Proc. R. Soc. London, Ser. A*, 332, 443–471.
- Golombek, M. P., and N. T. Bridges (2000), Erosion rates on Mars and implications for climate change: Constraints from the Pathfinder landing site, *J. Geophys. Res.*, 105, 1841–1853.
- Golombek, M. P., J. A. Grant, L. S. Crumpler, R. Greeley, R. E. Arvidson, and the Athena Science Team (2005), Climate change from the Mars Exploration Rover landing sites: From wet in the Noachian to dry and desiccating since the Hesperian, *Lunar Planet. Sci.*, 36, 1539.
- Greeley, R., and J. D. Iversen (1985), *Wind as a Geological Process*, 333 pp., Cambridge Univ. Press, New York.
- Greeley, R., B. R. White, R. N. Leach, J. D. Iversen, and J. B. Pollack (1976), Mars: Wind friction speeds for particle movement, *Geophys. Res. Lett.*, 3, 417–420.
- Greeley, R., B. R. White, J. B. Pollack, J. D. Iversen, and R. N. Leach (1981), Dust storms on Mars: Considerations and simulations, *Spec. Pap. Geol. Soc. Am.*, 186, 101–121.
- Greeley, R., R. N. Leach, S. H. Williams, B. R. White, J. B. Pollack, D. H. Krinsley, and J. R. Marshall (1982), Rate of wind abrasion on Mars, *J. Geophys. Res.*, 87, 10,009–10,024.
- Greeley, R., S. H. Williams, and J. R. Marshall (1983), Velocities of wind-blown particles in saltation: Preliminary laboratory and field measurements, in *Eolian Sediments and Processes*, edited by M. E. Brookfield and T. S. Ahlbrandt, pp. 133–148, Elsevier, New York.
- Greeley, R., N. Lancaster, S. Lee, and P. Thomas (1992), Martian aeolian processes, sediment, and features, in *Mars*, edited by H. H. Kieffer et al., pp. 730–766, Univ. of Ariz. Press, Tucson.
- Greeley, R., N. T. Bridges, R. O. Kuzmin, and J. E. Laity (2002), Terrestrial analogs to wind-related features at the Viking and Pathfinder landing sites on Mars, *J. Geophys. Res.*, 107(E1), 5005, doi:10.1029/2000JE001481.
- Greeley, R., et al. (2004), Wind-related processes detected by the Spirit rover at Gusev Crater, Mars, *Science*, 305, 810–821.
- Herkenhoff, K. E., et al. (2004), Textures of the soils and rocks at Gusev Crater from Spirit's Microscopic Imager, *Science*, 305, 824–826.
- Iversen, J. D., and B. R. White (1982), Saltation threshold on Earth, Mars, and Venus, *Sedimentology*, 29, 111–119.
- Krinsley, D., R. Greeley, and J. B. Pollack (1979), Abrasion of windblown particles on Mars—Erosion of quartz and basaltic sand under simulated Martian conditions, *Icarus*, 39, 364–384.
- Laity, J. E. (1987), Topographic effects on ventifact development, Mojave Desert, California, *Phys. Geogr.*, 8, 113–132.
- Laity, J. E. (1992), Ventifact evidence for Holocene wind patterns in the east-central Mojave Desert, *Z. Geomorphol.*, 84, Suppl., 1–16.
- Laity, J. E. (1994), Landforms of aeolian erosion, in *Geomorphology of Desert Environments*, edited by A. D. Abrahams and A. J. Parsons, pp. 506–535, CRC Press, Boca Raton, Fla.
- Laity, J. E. (1995), Wind abrasion and ventifact formation in California, in *Desert Aeolian Processes*, edited by V. P. Tchakerian, pp. 295–321, CRC Press, Boca Raton, Fla.
- Liu, L., S. Gao, P. Shi, X. Li, and Z. Dong (2003), Wind tunnel measurements of adobe abrasion by blown sand: Profile characteristics in relation to wind velocity and sand flux, *J. Arid Environ.*, 53, 351–363.
- Malin, M. C. (1985), Abrasion rate observations in Victoria Valley, Antarctica: 340-day experiment, *Antarct. J. U. S.*, 19(5), 14–16.
- Malin, M. C., and K. S. Edgett (2000), Evidence for recent groundwater seepage and surface runoff on Mars, *Science*, 288, 2330–2335.
- Malin, M. C., and K. S. Edgett (2001), Mars Global Surveyor Mars Orbiter Camera: Interplanetary cruise through primary mission, *J. Geophys. Res.*, 106, 23,429–23,570.
- Malin, M. C., et al. (1998), Early views of the Martian surface from Mars Orbiter Camera of Mars Global Surveyor, *Science*, 279, 1681–1685.
- McCauley, J. F., C. S. Breed, F. El-Baz, M. I. Whitney, M. J. Grolrier, and A. W. Ward (1979), Pitted and fluted rocks in the Western Desert of Egypt: Viking comparison, *J. Geophys. Res.*, 84, 8222–8232.
- McKee, E. D. (Ed.) (1979), A study of global sand seas, *U.S. Geol. Surv. Prof. Pap.* 1052, 429 pp.
- Morris, R. V. (2004), Mineralogy at Gusev Crater from the Mossbauer Spectrometer on the Spirit Rover, *Science*, 305, 833–836.
- Mutch, T. A., R. E. Arvidson, A. B. Binder, E. A. Guinness, and E. C. Morris (1977), The geology of the Viking 2 landing site, *J. Geophys. Res.*, 82, 4452–4467.
- Needham, C. E. (1937), Ventifacts from New Mexico, *J. Sediment. Petrol.*, 7, 31–33.
- Phoreman, J. (2002), Wind tunnel studies of aeolian saltation threshold and dust storm triggering mechanisms with the use of high-speed video and specialized boundary-layer wind tunnels at atmospheric and Martian mean surface pressures, Masters thesis, 163 pp., Dep. of Mech. and Aeronaut. Eng., Univ. of Calif., Davis, Davis.
- Pollack, J. B., R. Haberle, R. Greeley, and J. Iversen (1976), Estimates of the wind speeds required for particle motion on Mars, *Icarus*, 29, 395–417.
- Routbort, J. L., R. O. Scattergood, and E. W. Kay (1980), Erosion of silicon single crystals, *J. Am. Ceram. Soc.*, 63, 635–640.
- Saffman, P. G. (1965), The lift on a small sphere in a slow shear flow, *J. Fluid Mech.*, 22, 385–400.
- Saffman, P. G. (1968), Corrigendum, *J. Fluid Mech.*, 31, 624.
- Scattergood, R. O., and J. L. Routbort (1983), Velocity exponent in solid-particle erosion, *J. Am. Ceram. Soc.*, 66, C184–C186.
- Schoewe, W. H. (1932), Experiments on the formation of wind-faceted pebbles, *Am. J. Sci.*, 24, 111–134.
- Sharp, R. P. (1948), Pleistocene ventifacts east of the Big Horn Mountains, Wyoming, *J. Geol.*, 57, 173–195.
- Sharp, R. P. (1964), Wind-driven sand in Caochella Valley, California, *Bull. Geol. Soc. Am.*, 75, 785–804.
- Sharp, R. P. (1980), Wind-driven sand in Caochella Valley, California: Further data, *Bull. Geol. Soc. Am.*, 91, 724–730.
- Soderblom, L. A., et al. (2004), Soils of Eagle Crater and Meridiani Planum at the Opportunity Rover landing site, *Science*, 306, 1723–1726.
- Suyres, S. W., et al. (2004), The Opportunity rover's Athena science investigation at Meridiani Planum, Mars, *Science*, 306, 1698–1703.
- Sullivan, R., et al. (2005), Aeolian processes at the Mars Exploration Rover Meridiani Planum landing site, *Nature*, 436, 58–61.
- Suzuki, T., and K. Takahashi (1981), An experimental study of wind abrasion, *J. Geol.*, 89, 23–36.
- Takeuchi, Y. (1980), Vertical profile and horizontal increase of drift-snow transport, *J. Glaciol.*, 26, 481–492.
- Tanaka, K. L., D. H. Scott, and R. Greeley (1992), Global stratigraphy, in *Mars*, edited by H. H. Kieffer et al., pp. 345–382, Univ. Ariz. Press, Tucson.
- Thomas, P. C., et al. (1999), Bright dunes on Mars, *Nature*, 397, 592–594.

- Tsoar, H., B. White, and E. Berman (1996), The effect of slopes on sand transport—Numerical modeling, *Landscape Urban Plann.*, **34**, 171–181.
- Ungar, J. E., and P. K. Haff (1987), Steady state saltation in air, *Sedimentology*, **34**, 289–299.
- Viking Lander Team (1978), The Martian landscape, *NASA Spec. Publ.*, SP-425, 160 pp.
- Ward, A. W. (1979), Yardangs on Mars: Evidence of recent wind erosion, *J. Geophys. Res.*, **84**, 8147–8166.
- White, B. R. (1979), Soil transport by winds on Mars, *J. Geophys. Res.*, **84**, 4643–4651.
- White, B. R. (1982), Two-phase measurements of saltating turbulent boundary layer, *Int. J. Multiphase Flow*, **8**, 459–473.
- White, B. R. (1986), Particle dynamics in two-phase flow, in *Encyclopedia of Fluid Mechanics*, pp. 240–282, Gulf, Houston, Tex.
- White, B. R., and J. C. Schulz (1977), Magnus effect in saltation, *J. Fluid Mech.*, **81**, 497–512.
- White, B. R., and H. Tsoar (1997), Slope effect on saltation over a climbing sand dune, *Geomorphology*, **599**, 1–22.
- White, B. R., R. Greeley, J. D. Iversen, and J. B. Pollack (1976), Estimated grain saltation in a Martian atmosphere, *J. Geophys. Res.*, **81**, 5643–5650.
- Williams, G. P. (1964), Some aspects of eolian saltation load, *Sedimentology*, **3**, 257–287.
- Wilshire, H. G., J. D. Nakata, and B. Hallet (1981), Field observations of the December 1977 wind storm, San Joaquin Valley, California, in *Desert Dust*, edited by T. J. Pewe, *Spec. Pap. Geol. Soc. Am.*, **186**, 233–251.
- Woodworth, J. B. (1894), Post-glacial aeolian action in southern New England, *Am. J. Sci.*, **47**, 63–71.
- Zimbelman, J. R. (2000), Non-active dunes in the Acheron Fossae region of Mars between the Viking and Mars Global Surveyor eras, *Geophys. Res. Lett.*, **27**, 1069–1072.
- 
- N. T. Bridges and G. R. Wilson, Jet Propulsion Laboratory, MS 183-501, 4800 Oak Grove Dr., Pasadena, CA 91109, USA. (nathan.bridges@jpl.nasa.gov)
- E. E. Eddlemon, Department of Geological Sciences, Arizona State University at NASA-Ames Research Center, Moffett Field, CA 94035, USA.
- R. Greeley, Department of Geological Sciences, Arizona State University, Tempe, AZ 85287-1404, USA.
- C. J. Meyer, Department of Geological Sciences, Ohio University, Athens, OH 45701, USA.
- J. Phoreman, BAE Systems, 5140 West Goldleaf Circle, Los Angeles, CA 90056, USA.
- B. R. White, Department of Mechanical Engineering, University of California, Davis, Davis, CA 95616-5294, USA.